Research article

Geoenergy

https://doi.org/10.1144/geoenergy2024-022 | Vol. 3 | 2025 | geoenergy2024-022

Impact of sedimentological heterogeneity on subsurface storage in net-transgressive, shallow-marine sandstones: Cliff House Sandstone, New Mexico, USA

Xiaowen Wu[1], Gary J. Hampson[1*], Carl Jacquemyn[1], Shakhawat Hossain[1,2], Matthew D. Jackson[1], Dmytro Petrovskyy[1,3] and Sebastian Geiger[3]

[1] Department of Earth Science and Engineering, Imperial College London, London SW7 2AZ, UK
[2] Department of Geology, University of Dhaka, Dhaka 1000, Bangladesh
[3] Department of Geoscience and Engineering, Delft University of Technology, 2600 AA Delft, The Netherlands
GJH, 0000-0003-2047-8469
* Correspondence: g.j.hampson@imperial.ac.uk

Abstract: Net-transgressive, shallow-marine sandstone reservoirs overlain by thick mudstone seals are prime candidates for storage of CO_2, H_2 and thermal energy. Although these reservoirs have high net-to-gross ratios, analogous outcrops demonstrate a wide range of sedimentological heterogeneities that are sampled only sparsely or at low resolution in subsurface data. We use a combination of outcrop data, sketch-based reservoir modelling and flow diagnostics to assess the impact of sedimentological heterogeneities on subsurface storage.

The Cliff House Sandstone outcrop example comprises wave-dominated shoreface sandstones arranged in aggradationally-to-retrogradationally stacked parasequences, which overlie and pass up depositional dip into mudstone-dominated coastal plain, lagoonal and tidal flat deposits that encase channelized tidal and tidally influenced fluvial sandbodies. Reservoir models of this outcrop example demonstrate that effective horizontal permeability, flow patterns and displacement, and stratigraphic trapping potential are controlled by: (1) the packaging of shoreface sandstones into laterally extensive parasequences bounded by offshore mudstones; (2) the spatial distribution, connectivity and permeability of channelized sandbodies; and (3) the localized connections between channelized sandbodies and shoreface sandstones. The last two parameters are likely to be poorly constrained in subsurface seismic and well data, and their potential effects require evaluation in reservoir modelling studies.

Received 16 July 2024; **revised** 11 February 2025; **accepted** 19 February 2025

Net-transgressive, shallow-marine sandstones commonly form laterally extensive sheets of variable continuity and internal stratigraphic complexity that record overall shoreline retreat and are overlain by thick successions of offshore mudstones (e.g. Cattaneo and Steel 2003; Hampson *et al.* 2009). The net-transgressive sandstones and overlying mudstones thus constitute a reservoir–seal pair that is potentially well suited for storage of fluids in the subsurface. For example, the net-transgressive Lower Cretaceous Vlieland Sandstone of the onshore and offshore Netherlands hosts oil and gas accumulations (Goh 1993), geothermal energy resources (Mijnlieff 2020) and forms a potential CO_2 storage play (Siebels *et al.* 2022). Although net-transgressive sandstone reservoirs commonly have a high net-to-gross ratio, they can exhibit complex stratigraphic architectures characterized by stacking of multiple sandbody types that vary in their geometry, distribution and preservation (e.g. Donselaar 1989; Olsen *et al.* 1999; Cattaneo and Steel 2003; Sixsmith *et al.* 2008; Jordan *et al.* 2016). The resulting sedimentological and stratigraphic heterogeneity can strongly influence subsurface fluid flow, as evidenced by unexpectedly complex production behaviour and poor recovery in oil and gas reservoirs (e.g. Sixsmith *et al.* 2008; Copestake 2023).

In this study, we use data from a well-documented outcrop example of a net-transgressive shallow marine sandstone, the Cliff House Sandstone exposed in Chaco Culture National Historical Park, New Mexico, USA (Donselaar 1989; Jordan *et al.* 2016), to investigate subsurface fluid flow and storage potential. In Chaco Culture National Historical Park, variably stacked fluvial, tidal and shoreface sandbodies constitute approximately 90% of the Cliff House Sandstone (Jordan *et al.* 2016). Extensive cliff face exposures allow the three-dimensional (3D) geometry, distribution and spatial organization of sandbodies and intervening mudstone-rich deposits to be reconstructed in this outcrop example with a much higher degree of certainty than in subsurface storage units, which are sampled only sparsely or at low resolution using well and seismic data (e.g. Howell *et al.* 2014). The heterogeneity and distribution of porosity, permeability and other rock properties in subsurface reservoirs strongly influence fluid flow patterns, controlling drainage and recovery of hydrocarbons (e.g. Weber and Van Geuns 1990; Tyler and Finley 1991), the injectivity, dispersal and storage capacity of CO_2 (e.g. Flett *et al.* 2007; Gibson-Poole *et al.* 2009; Krevor *et al.* 2023), and geothermal energy recovery and efficiency (e.g. Crooijmans *et al.* 2016; Wang *et al.* 2021). The aims of this paper are threefold: (1) to develop a suite of reservoir models that capture stratigraphic and sedimentological heterogeneities, and related uncertainties, in the Cliff House Sandstone outcrop example; (2) to identify the key sedimentological heterogeneities that control fluid flow and their characteristic flow patterns; and (3) to consider the implications for subsurface fluid migration and storage in net-transgressive, shallow-marine sandstones. We address these aims by using a geologically intuitive, sketch-based reservoir modelling approach combined with computationally efficient, single-phase flow diagnostics, both of which are implemented in the Open Source research code, Rapid Reservoir Modelling (RRM; Costa Sousa *et al.* 2020; Jacquemyn *et al.* 2021; Petrovskyy *et al.* 2023). The resulting models are intended to investigate the general storage potential of the Cliff House sandstone outcrop example, rather than a site-specific storage plan. For this reason, structural elements such as faults and tectonic

dip are not considered in the models, so that the effects of sedimentological heterogeneity are not obscured. Our approach allows the effects of sedimentological heterogeneity to be investigated in a fast and efficient manner, prior to more detailed flow simulations that are specific to the subsurface fluids and storage site under investigation.

Geological context and stratigraphic architecture of Cliff House Sandstone

The Cliff House Sandstone records approximately 170 km of shoreline retreat over a period of *c.* 4 Myr (Fig. 1; Molenaar 1983). The unit consists of a retrogradationally stacked succession of marginal-marine and shallow-marine deposits, recording the development of regressive strandplain and wave-dominated deltaic shorelines that alternated with transgressive barrier islands (Sears *et al.* 1941; Palmer and Scott 1984; Donselaar 1989; Olsen *et al.* 1999; Jordan *et al.* 2016). It represents deposition along a NW–SE-trending stretch of shoreline that fringed part of a broad embayment ('Utah Bight') along the western margin of the Cretaceous Western Interior Seaway (Fig. 1; Kauffman and Caldwell 1993; Van Cappelle *et al.* 2018). Shoreline orientation and patterns of shoreline retreat reflect a combination of tectonic subsidence, sea-level fluctuations, and sediment supply from the Sevier fold-and-thrust belt to the west and Mogollon Highlands to the SW (Fig. 1; e.g. Krystinik and DeJarnett 1995; Lawton *et al.* 2003; Painter and Carrapa 2013; Szwarc *et al.* 2015; Van Cappelle *et al.* 2018; Li and Aschoff 2022). The combination of these controls is reflected in the locally variable thickness (up to 240 m) and stratigraphic-architectural style of the Cliff House Sandstone (e.g. Fig. 1) and of net-transgressive sandstone successions more generally. Thick successions comprising vertically stacked, regressive–transgressive sandstone tongues (parasequences) separated locally by mudstones are developed where the net-transgressive shoreline trajectory (i.e. overall angle of shoreline retreat) was relatively steep (e.g. Jordan *et al.* 2016; cf. Cattaneo and Steel 2003; Sixsmith *et al.* 2008). In contrast, thin successions of erosionally amalgamated sandstones in which mudstones are poorly preserved characterize relatively shallow net-transgressive shoreline trajectories (cf. Cattaneo and Steel 2003; Sixsmith *et al.* 2008).

The upper part of the Cliff House Sandstone, which is Middle Campanian in age, is exposed in deeply incised canyons in Chaco Culture National Historical Park, NW New Mexico, USA, resulting in 3D outcrop control (Scott *et al.* 1984; Donselaar 1989; Jordan *et al.* 2016) (Fig. 2). Here, the Cliff House Sandstone contains 11 parasequences of shoreface-shelf sandstones (wave-dominated facies association in Table 1) that are aggradationally-to-retrogradationally stacked into four parasequence sets (Jordan *et al.* 2016). Each shoreface-shelf sandstone parasequence is laterally extensive along the (NW–SE) depositional strike of the palaeoshoreline, interfingers with and grades into offshore mudstones down depositional dip (towards NE), and pinches out into mudstone-dominated coastal plain deposits and/or channelized tidal sandbodies up depositional dip (towards SW) (continental and tide-dominated facies associations in Table 1; Fig. 2; Jordan *et al.* 2016; cf. Sixsmith *et al.* 2008). Internally, shoreface-shelf sandstone parasequences contain a shallowing-upward facies succession that comprises, from base to top: offshore mudstones, distal lower shoreface sandstone and mudstone heteroliths, proximal lower shoreface sandstones, and top-truncated upper shoreface and foreshore sandstones (Table 1; Fig. 2; Jordan *et al.* 2016). Each parasequence is bounded at its base and top by laterally extensive, wave ravinement surfaces that are interpreted to have been cut by wave erosion during transgression (Fig. 2; Jordan *et al.* 2016; cf. Swift 1968; Sixsmith *et al.* 2008). Channelized tidal sandbodies (facies T1 in Table 1) erode into, and define the updip termination of, most shoreface-shelf sandstone tongues. In the latter examples, the basal erosion surfaces of the channelized tidal sandbodies are interpreted as tidal ravinement surfaces (Fig. 2; Jordan *et al.* 2016; cf. Swift 1968; Sixsmith *et al.* 2008). Tidally influenced fluvial channel-fill sandbodies (facies T2 in Table 1) are located below and palaeolandward of the lower three shoreface-shelf sandstone tongues (Fig. 2; Jordan *et al.* 2016).

Dataset and methodology

We use three correlation panels along major, WSW–ENE-oriented canyons (Fig. 2), oblique to depositional dip, to construct a suite of

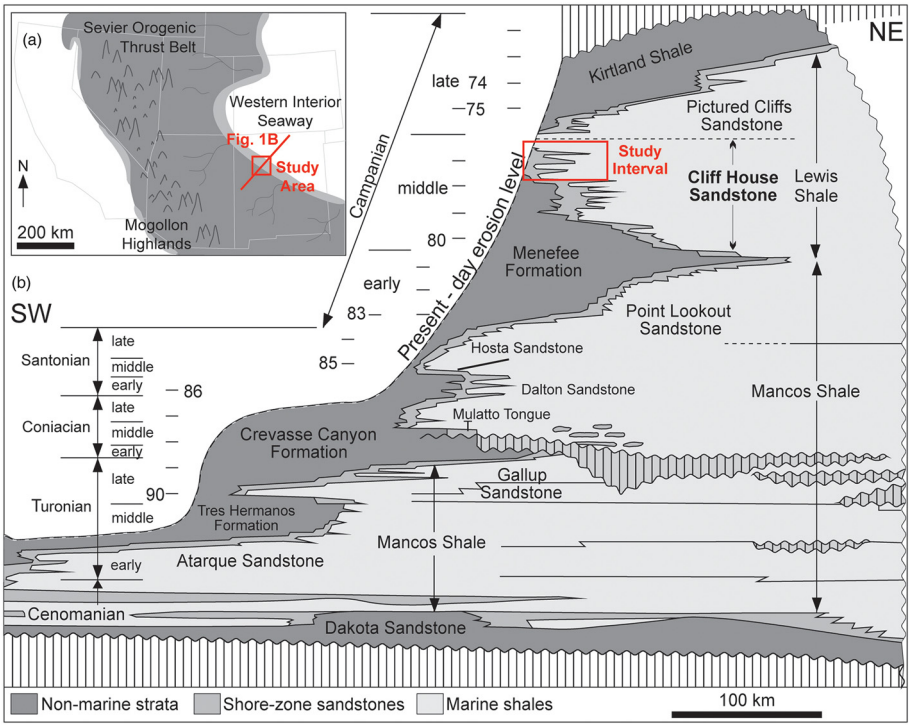

Fig. 1. Geological context of the Cliff House Sandstone. (**a**) Palaeogeographic reconstruction of the southwestern Western Interior Seaway during the Late Cretaceous (at approximately 75 Ma), including the approximate location of the Cliff House Sandstone shoreline (Molenaar 1983; Donselaar 1989), the line of cross section (Fig. 1b), and the location of the study area (Fig. 2). (**b**) Summary chronostratigraphic diagram of Cretaceous strata in the San Juan Basin, New Mexico and Colorado, USA. Cretaceous stages and approximate ages (in Ma) are indicated. The upper part of the Cliff House Sandstone, which is exposed in Chaco Cultural National Historical Park (Fig. 2), is highlighted. Source: (b) after Molenaar 1983; Jordan *et al.* 2016.

Table 1. Summary of facies and facies associations in the Cliff House Sandstone outcrop example (after Jordan et al. 2016)

Facies association	Facies code	Facies	Sedimentary structures	Geometry	Porosity and permeability
Continental facies association	Cp1	Undifferentiated coastal plain and lagoon	Micaceous mudstones, siltstones and rare fine-grained sandstones. Abundant carbonaceous plant material. Bioturbation Index (BI) = 0.	Mudstone-dominated sheets: 0.8 to >10 m thick, <10 km dip and strike extent	(1) $\varphi = 10\%$, $k_h = k_v = 0.001$ mD; or (2) $\varphi = 20\%$, $k_h = 20$ mD, $k_v = 0.02$ mD
Tide-dominated facies association	T1	Tidal channel-fill	Poor to moderately well sorted, fine- to lower coarse-grained sandstone. Bidirectional trough and tabular cross bedding, with occasional silty-clay drapes. Current-ripple cross-lamination and mud rip-up clasts. BI = 1.	Sandstone lenses: 1–20 m thick, 3–6 km dip extent, >10 km strike extent	$\varphi = 27\%$, $k_h = 2000$ mD, $k_v = 200$ mD
	T2	Tidally influenced fluvial channel-fill	Poor to moderately sorted, fine- to medium-grained sandstone. Abundant cross bedding with carbonaceous drapes and current-ripple cross-lamination, with water escape structures and mud rip-up clasts. BI = 3.	Sandstone ribbons: 1–20 m thick, 1–4 km dip extent, channel belts >10 km strike extent	(1) $\varphi = 27\%$, $k_h = 2000$ mD, $k_v = 200$ mD; or (2) $\varphi = 28\%$, $k_h = k_v = 4000$ mD
	T3	Tidal flats	Intercalated fine- to medium-grained sandstones, siltstones and mudstones. Sandstones are wave-ripple and current-ripple cross-laminated, with abundant carbonaceous material. Flaser and lenticular bedding throughout. BI = 2.	Heterolithic sheets: 1–5 m thick, 100–200 m dip and strike extent	(1) $\varphi = 10\%$, $k_h = k_v = 0.001$ mD; or (2) $\varphi = 20\%$, $k_h = 20$ mD, $k_v = 0.02$ mD
Wave-dominated facies association	W1	Foreshore	Moderately sorted, upper fine- to medium-grained sandstone. Planar-parallel lamination and low-angle lamination. BI = 3.	Poorly preserved sandstone sheets: 1–2 m thick, 1–2 km in dip extent, 10 s km strike extent	$\varphi = 27\%$, $k_h = 2000$ mD, $k_v = 2000$ mD
	W2	Upper shoreface	Moderately sorted, upper fine- to medium-grained sandstone. Trough and tabular cross-beds. BI = 3.	Sandstone sheets: 1–2 m thick, 1–2 km in dip extent, 10 s km strike extent	$\varphi = 27\%$, $k_h = 2000$ mD, $k_v = 2000$ mD
	W3	Proximal lower shoreface	Amalgamated beds of well sorted, fine-grained sandstone. Swaley and hummocky cross-stratification, with rare wavy lamination, planar lamination and low-angle lamination. BI = 3–4.	Sandstone sheets: 1–20 m thick, <10 km dip extent, 10 s km strike extent	$\varphi = 24\%$, $k_h = 200$ mD, $k_v = 20$ mD
	W4	Distal lower shoreface	Non-amalgamated beds of well sorted, fine-grained sandstone interbedded with siltstone and mudstone. Sandstones are hummocky cross-stratified with rare wave-ripple cross-lamination. BI = 3.	Heterolithic tabular wedges: 1–5 m thick, <5 km dip extent, 10 s km strike extent	(1) $\varphi = 10\%$, $k_h = k_v = 0.001$ mD; or (2) $\varphi = 20\%$, $k_h = 20$ mD, $k_v = 0.02$ mD
	W5	Offshore shales	Interbedded siltstones and mudstones with rare, thin fine-grained sandstone beds. Planar, parallel lamination. Sandstones contain wavy lamination and ripple cross-lamination.	Mudstone-dominated tabular wedges: 1–5 m thick, <5 km dip extent, 10 s km strike extent	(1) $\varphi = 10\%$, $k_h = k_v = 0.001$ mD; or (2) $\varphi = 20\%$, $k_h = 20$ mD, $k_v = 0.02$ mD
	D1	Mouth bars	Interbedded upper fine-grained sandstone, siltstone and mudstone. Sandstones contain hummocky and swaley cross-stratification, wave- and current-ripple cross-lamination, planar-parallel lamination and low-angle inclined lamination. Mud rip-up clasts are common.	Discontinuous channelized bodies: 1–4 m thick	$\varphi = 24\%$, $k_h = 200$ mD, $k_v = 2$ mD

Porosity and permeability values assigned to each facies are based on North Sea reservoirs, after Goh (1993), Livera (1989) for facies Cp1, T1–T3 (their table 2), Jackson *et al.* (2009) for facies W1–W5 (their table 1), and Onyenanu *et al.* (2019) for k_v/k_h ratio of facies D1 (their figure 14). Bioturbation intensity is described using the BI scheme of Taylor and Goldring (1993).

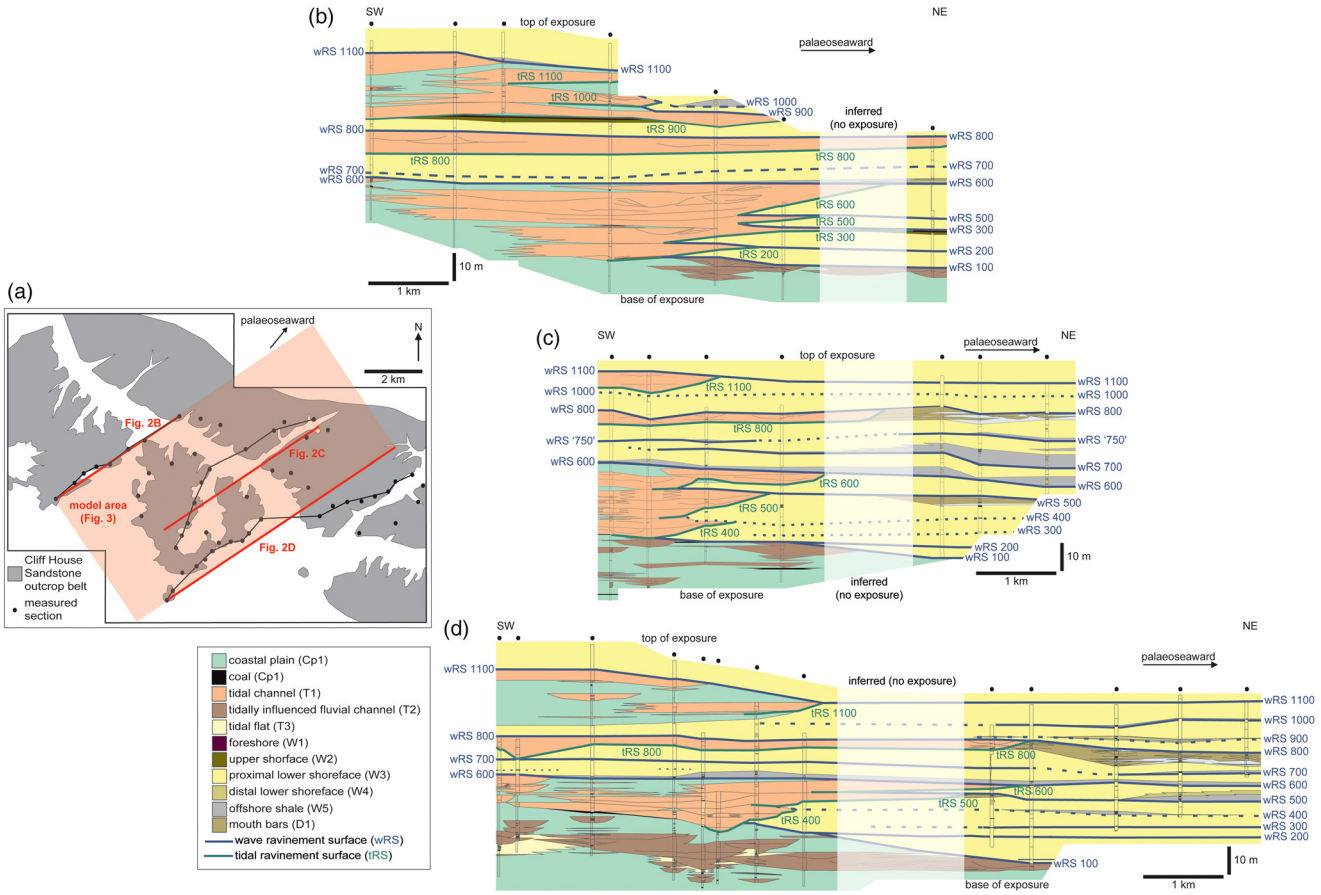

Fig. 2. Summary of outcrop dataset from Chaco Culture National Historical Park, New Mexico, USA. (**a**) Map showing Cliff House Sandstone outcrop extent in the park, showing locations of measured sections, correlation panels (thin black lines between measured sections), planar approximations of correlation panels used to construct sketch-based models (thick red lines), and area represented in sketch-based models (semi-transparent red rectangle). (**b–d**) Correlation panels oriented oblique to depositional dip, from SW (palaeolandward) to NE (palaeoseaward). The datum for the panels is the most widespread transgressive surface, wRS 600. Panels are located in (a). Source: after Jordan *et al.* (2016).

reservoir models (Fig. 3). The three correlation panels are part of the dataset documented in Jordan *et al.* (2016), and share a stratigraphic framework that is also based on a WNW–ESE-oriented correlation panel, oblique to depositional dip. The WSW–ENE-oriented correlation panels are treated as three parallel planes (Fig. 2), to facilitate their use in sketch-based model construction. There is little uncertainty in the distribution and internal architecture of shoreface-shelf sandstone tongues between the three correlation panels, because the sandstone tongues are laterally extensive along depositional strike (wave-dominated facies association in Table 1). In contrast, there is uncertainty in the geometry and distribution of channelized tidal and tidally influenced fluvial sandbodies (facies T1 and T2 in Table 1) between the three panels.

Modelled heterogeneities

In order to assess the influence of sedimentological heterogeneity on subsurface fluid migration and storage in the Cliff House Sandstone example, we selected six heterogeneities for investigation (Table 2). Three of these heterogeneities reflect the geometry, distribution and spatial organization of facies units (Table 1), while three further heterogeneities reflect the values of porosity and permeability assigned to selected facies. The six heterogeneities are selected to assess the impact of uncertainties in a typical subsurface dataset and/or the outcrop dataset, as outlined below.

(1) The plan-view distribution and geometry of tidally influenced fluvial channel-fill sandbodies (facies T2) is uncertain in regions between the three correlation panels along major, WSW–ENE-oriented canyons (Fig. 2). We develop three different interpreted scenarios of the orientation, width and plan-view distribution of these channelized sandbodies, each of which is consistent with palaeocurrent data in figure 6C of Jordan *et al.* (2016) (Table 1). Palaeocurrents exhibit a wide spread of orientations, with mean palaeoflow orientations towards the SW (N237°) and north (N006°) in lower and upper units of tidally influenced fluvial channel-fill sandbodies (figure 6C of Jordan *et al.* 2016). Channelized sandbodies with similar vertical positions relative to a widespread datum (wave ravinment surface wRS 600 in Fig. 2) are correlated between the three panels. Scenario 1 contains three channelized sandbodies that represent channel belts: the oldest is oriented east–west (Fig. 4a), overlain by a second north–south-oriented channelized sandbody and a third SW–NE-oriented channelized sandbody (Fig. 4b). The youngest sandbody does not extend to the northwestern side of the study area, where it is eroded by overlying tidal channels. Scenario 2 also contains three channelized sandbodies representing channel belts. The oldest sandbody is oriented SW–NE, the second sandbody is sinuous with a mean NW–SE orientation (Fig. 4c), while the youngest sandbody is similar to that in Scenario 1 (Fig. 4d). Scenario 3 contains four channel-belt sandbodies; the first, second and third sandbodies are oriented NW–SE and stacked with lateral offsets towards the SW and NE (Fig. 4e, f), while the youngest sandbody is similar to that in Scenario 1 (Fig. 4f). Channel-belt sandbodies in each scenario are 5–7 km wide

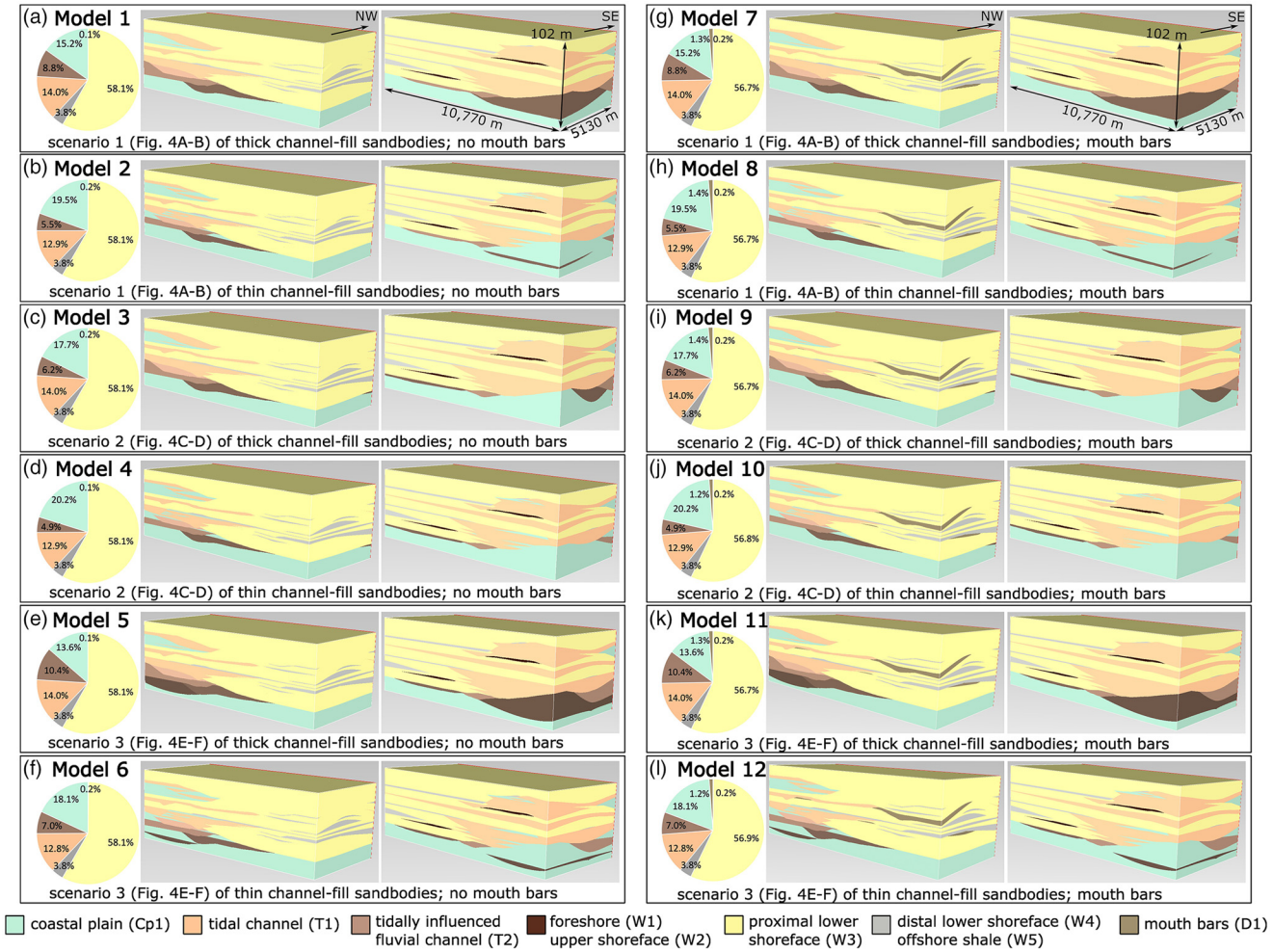

Fig. 3. Comparison of facies architecture and facies proportions in models 1–12 (Table 3). (**a–l**) A pie chart of facies proportions, a SE-facing 3D perspective view, and a NW-facing 3D perspective view are shown for each model.

with width:thickness ratios of 5–30, which are typical of deltaic distributaries (Gibling 2006).

(2) Two interpretations are developed for the thickness and vertical connectivity of tidal (facies T1) and tidally influenced fluvial (facies T2) channel-fill sandbodies in between the three cliff-face correlation panels (Table 1). The channel-belt sandbodies in the three scenarios described above are either stacked vertically to form a larger multistorey body (Fig. 4), or are separated vertically by intervals of mudstone-dominated coastal plain deposits. In combination with their plan-view distribution, the thickness and vertical connectivity of channelized sandbodies are expected to influence the proportion of tidal and tidally influenced fluvial channel-fill sandstone facies T1 and T2, and, by corollary, the proportion of non-channelized continental facies Cp1 and T3. The connectivity of channelized sandbodies has also been shown to control fluid flow patterns and recovery in hydrocarbon reservoirs (Jones *et al.* 1995; Larue and Hovadik 2006; Villamizar *et al.* 2015).

(3) Mouth bar deposits are treated either as distinct, localized facies bodies (facies D1) developed at the down-dip

Table 2. Summary of investigated sedimentological heterogeneities, and their representation in different models

Sedimentological heterogeneity	Model settings
1. Plan-view distribution and geometry of tidally influenced fluvial channel-fill sandbodies (facies T2)	Three scenarios of channel distribution (1–3) are modelled, based on different correlations of channel-fill sandbodies between cliff-face panels (Fig. 3)
2. Thickness and vertical connectivity of tidal (facies T1) and tidally influenced fluvial (facies T2) channel-fill sandbodies	Channel-fill sandbodies developed at different stratigraphic levels are modelled as: (1) thick, vertically connected units; and (2) thin units that are vertically separated by mudstone-dominated coastal plain deposits
3. Distinction of mouth bar deposits (facies D1) from proximal lower shoreface deposits (facies W3)	Mouth bar deposits are modelled as: (1) distinct, localized facies bodies; or (2) part of proximal lower shoreface facies belts
4. Porosity and permeability of mudstone-dominated coastal plain (facies Cp1) and tidal flat (facies T3) deposits	Coastal plain and tidal flat deposits are assigned: (1; non-reservoir) $\varphi = 10\%$, $k_h = k_v = 0.001$ mD; and (2; reservoir) $\varphi = 20\%$, $k_h = 20$ mD, $k_v = 0.02$ mD
5. Porosity and permeability of tidally influenced fluvial channel-fill sandbodies (facies T2)	Tidally influenced fluvial channel-fill sandbodies are assigned: (1) $\varphi = 27\%$, $k_h = 2000$ mD, $k_v = 200$ mD; and (2) $\varphi = 28\%$, $k_h = k_v = 4000$ mD
6. Porosity and permeability of distal lower shoreface (facies W4) and offshore (facies W5) deposits	Distal lower shoreface and offshore deposits are assigned: (1; non-reservoir) $\varphi = 10\%$, $k_h = k_v = 0.001$ mD; and (2; reservoir) $\varphi = 20\%$, $k_h = 20$ mD, $k_v = 0.02$ mD

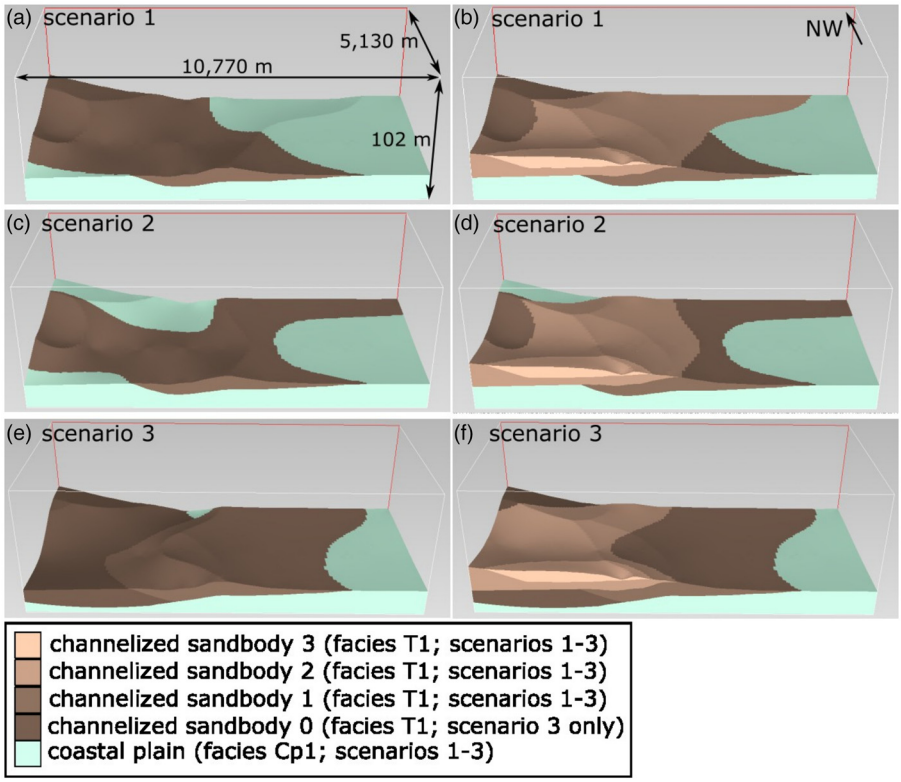

Fig. 4. SE-facing 3D perspective views of coastal plain (facies Cp1) and tidally influenced fluvial channel-belt sandbodies (facies T2) in the lower part of selected models, illustrating different interpreted scenarios of channel-belt sandbody distribution and geometry: (**a**, **b**) scenario 1 (models 1, 2, 7 and 8); (**c**, **d**) scenario 2 (models 3, 4, 9 and 10); and (**e**, **f**) scenario 3 (models 5, 6, 11 and 12) (Table 3; Fig. 3).

terminations of tidally influenced fluvial channel-fill sandstones (facies T2) or are grouped together with proximal lower shoreface facies belts (facies W3) (Table 1). These two contrasting treatments are considered to reflect uncertainty in the penetration and subsequent identification of localized mouth bar deposits by wells in the subsurface.

(4) Coastal plain (facies Cp1) and tidal flat (facies T3) deposits are relatively poorly exposed in the Cliff House Sandstone outcrops, and the two facies are grouped together in this study. Both facies are dominated by mudstones, but contain subordinate sandstones and siltstones (Table 1). In hydrocarbon reservoir studies, the two facies have been considered either as non-reservoir deposits ($\phi = 10\%$, $k_h = k_v = 0.001$ mD) (e.g. Livera 1989) or as poor-quality reservoir deposits ($\phi = 20\%$, $k_h = 20$ mD, $k_v = 0.02$ mD) (e.g. Abbots and Van Kuijk 1997; Colombera and Mountney 2021) (Table 2).

(5) Tidally influenced fluvial channel-fill sandbodies (facies T2) are comparable in their grain-size and textural characteristics as tidal channel-fill sandbodies (facies T1) (Table 1). We consider two interpretations, one in which the two facies are assigned the same reservoir quality ($\phi = 27\%$, $k_h = 2000$ mD, $k_v = 200$ mD) and one in which tidally influenced fluvial channel-fill sandbodies (facies T2) are assigned higher reservoir properties ($\phi = 28\%$, $k_h = k_v = 4000$ mD) (Table 2). Such differences in reservoir quality between channelized sandbodies have been demonstrated to influence recovery in hydrocarbon reservoirs (e.g. Jones *et al.* 1995).

(6) Distal lower shoreface (facies W4) and offshore (facies W5) deposits are also grouped together in this study. The former comprise interbedded fine-grained sandstones, siltstones and mudstones, while the latter is dominated by mudstones (Table 1). Both facies contain sandstone beds with steep-sided erosional scours or gutter casts at their base (Jordan *et al.* 2016), which can enhance sandstone connectivity and effective permeability (Onyenanu *et al.* 2019). The two facies are therefore considered either as non-reservoir deposits ($\phi = 10\%$, $k_h = k_v = 0.001$ mD) or as poor-quality reservoir deposits ($\phi = 20\%$, $k_h = 20$ mD, $k_v = 0.02$ mD) (Table 2).

We do not vary the porosity and permeability of proximal lower shoreface (facies W3), upper shoreface (facies W2), foreshore (facies W1) and tidal channel-fill (facies T1) deposits (Tables 1 and 2). Therefore, the impact of variations in these properties on reservoir character and behaviour is not investigated in our study. Additional heterogeneities at small (centimetre-to-decametre) scales, which are important in generating differences in relative permeability and capillary entry pressure during multiphase flow (e.g. Saadatpoor *et al.* 2009; Gershenzon *et al.* 2016; Jackson and Krevor 2020), can aid trapping of CO_2 and H_2, for example. Consideration of these heterogeneities lies beyond the scope of this work, but is the focus of ongoing work.

Model design

Twelve models have been constructed of the Cliff House Sandstone (Fig. 3), representing all possible combinations of the interpreted scenarios for heterogeneities at large length scales that impact the geometry, distribution and spatial organization of facies bodies (labelled 1–12 in Table 3). Each of the 12 models has eight sets of porosity and permeability values assigned to it, representing all possible combinations of the interpreted scenarios for heterogeneities at relatively small length scales that are represented implicitly by the values of porosity and permeability assigned to facies Cp1/T3, T2 and W4/W5 (labelled A–H in Table 4). Thus, a suite of 96 models and porosity-permeability sets (labelled 1A–H through to 12A–H) were used (Tables 3 and 4). This suite constitutes a full factorial experimental design (Box *et al.* 1978).

Model construction, dimensions and grids

The 12 models were constructed using a sketch-based approach that allows geological concepts and scenarios to be rapidly and intuitively captured by non-experts, and which is implemented in

Table 3. Settings for sedimentological heterogeneities that impact the geometry, distribution and spatial organization of facies units in models 1–12 (Fig. 2)

Sedimentological heterogeneity	Model setting	Model number											
		1	2	3	4	5	6	7	8	9	10	11	12
1. Plan-view distribution and geometry of tidally influenced fluvial channel-fill sandbodies (facies T2)	Scenario 1 (Fig. 3a, b)	×	×					×	×				
	Scenario 2 (Fig. 3c, d)			×	×					×	×		
	Scenario 3 (Fig. 3e, f)					×	×					×	×
2. Thickness and vertical connectivity of tidal (facies T1) and tidally influenced fluvial (facies T2) channel-fill sandbodies	Thick, vertically connected channel-fill sandbodies	×		×		×		×		×		×	
	Thin channel-fill sandbodies vertically separated by mudstone-dominated coastal plain deposits		×		×		×		×		×		×
3. Distinction of mouth bar deposits (facies D1) from proximal lower shoreface deposits (facies W3)	Mouth bar deposits modelled as distinct, localized facies bodies							×	×	×	×	×	×
	Mouth bar deposits modelled as part of proximal lower shoreface facies belts	×	×	×	×	×	×						

Table 4. Settings for sedimentological heterogeneities that impact the values of porosity and permeability assigned to facies in models 1–12 (Fig. 2)

Sedimentological heterogeneity	Model setting	Model number							
		1–12A	1–12B	1–12C	1–12D	1–12E	1–12F	1–12G	1–12H
4. Porosity and permeability of mudstone-dominated coastal plain (facies Cp1) and tidal flat (facies T3) deposits	Non-reservoir: $\varphi = 10\%$, $k_h = k_v = 0.001$ mD	×		×	×	×			
	reservoir: $\varphi = 20\%$, $k_h = 20$ mD, $k_v = 0.02$ mD		×				×	×	×
5. Porosity and permeability of tidally influenced fluvial channel-fill sandbodies (facies T2)	$\varphi = 27\%$, $k_h = 2000$ mD, $k_v = 200$ mD	×	×	×			×		
	$\varphi = 28\%$, $k_h = k_v = 4000$ mD				×	×		×	×
6. Porosity and permeability of distal lower shoreface (facies W4) and offshore (facies W5) deposits	Non-reservoir: $\varphi = 10\%$, $k_h = k_v = 0.001$ mD			×		×	×		×
	reservoir: $\varphi = 20\%$, $k_h = 20$ mD, $k_v = 0.02$ mD	×	×		×			×	

the Open Source research code, RRM (Costa Sousa *et al.* 2020; Jacquemyn *et al.* 2021). Geological architectures and heterogeneities (e.g. sequence stratigraphic surfaces, facies boundaries) are represented by surfaces (cf. Denver and Phillips 1990; Hamilton and Jones 1992) that define and bound geological domains (cf. Pyrcz *et al.* 2005; Caumon *et al.* 2009; Sech *et al.* 2009; Ruiu *et al.* 2016; Jacquemyn *et al.* 2019). Surfaces and surface-bounded geological domains are generated and manipulated using Sketch-Based Interface and Modelling (SBIM) methods that were developed for non-geological CAD and CFD applications. Operators that necessitate geological viability control interactions between SBIM-generated surfaces.

Our sketch-based modelling approach allows surfaces to be sketched in any order (Jacquemyn *et al.* 2021), although we follow the approach taken by Jackson *et al.* (2022) and Alshakri *et al.* (2023) in constructing comparable suites of sketch-based models. To ensure consistent and rapid model construction, surfaces that are shared across all 12 models were sketched initially and then reused. Surfaces that define heterogeneities that impact the geometry and distribution of facies units in different models (Table 3) are sketched later. Laterally extensive stratigraphic surfaces of relatively simple 3D geometry, including wave ravinement and tidal ravinement surfaces, were sketched in and linearly extruded between each cliff-face panel (Costa Sousa *et al.* 2020; Jacquemyn *et al.* 2021). More geometrically complex and less extensive surfaces, including the erosional bases of channelized, tidally influenced fluvial sandbodies (facies T2; Fig. 4), are sketched in one cliff-face panel and their cross-sectional geometries then extruded along a plan-view trajectory (Costa Sousa *et al.* 2020; Jacquemyn *et al.* 2021).

Each model has dimensions of 10 770 m (NE–SW) × 5130 m (NW–SE) × 102 m (thickness), and is visualized with a vertical exaggeration of ×35 (Fig. 3). Since our focus is on investigating the effects of sedimentological heterogeneity, structural elements such as faults and tectonic dip are not considered in the models. Models are generated without reference to an underlying grid. Once the model has been generated, a grid is then created to visualize the models (e.g. Fig. 3; Jacquemyn *et al.* 2021) or to perform numerical calculations (Petrovskyy *et al.* 2023). In the latter context, grid-cell size and grid resolution are discussed below.

Visual inspection of the sketch-based models confirms consistency between the modelled stratigraphic architectures (Figs 3, 4) and the underlying geological data and interpretations (Fig. 2). The modelled architectures thus represent the combinations and settings of heterogeneities outlined in Table 3.

Flow diagnostics

Calculations of pore volume are directly obtained from the sketched models after assigning porosity and permeability values to each facies (Table 1). Our implementation of sketch-based reservoir modelling is integrated with computationally efficient flow diagnostics, which allow key flow properties and behaviours to be assessed rapidly using controlled numerical experiments that rely on a reduced-physics, single-phase pressure solution (Shahvali *et al.* 2012; Møyner *et al.* 2014; Rasmussen and Lie 2014; Lie *et al.* 2015). The fundamental governing equations in flow diagnostics are based on Darcy's law and assume incompressible single-phase flow, absence of gravity and mass conservation (Møyner *et al.* 2014; Rasmussen and Lie 2014; Lie *et al.* 2015); Petrovskyy *et al.* (2023) provide detailed documentation of how flow diagnostics are implemented in the RRM code. Flow diagnostic outputs include the time of flight and stationary distribution of tracer fluid obtained from a steady-state pressure field for a given combination of fluid injection and offtake (production) boundary conditions (Petrovskyy *et al.* 2023). Flow paths through connected, highly permeable facies are highlighted by the time-of-flight output.

An orthogonal grid is used for flow diagnostic calculations, to ensure numerical stability (Petrovskyy *et al.* 2023). Grid cells measure 107.7 m (NE–SW) × 51.3 m (NW–SE) × 1.02 m (thickness), and there are 1 000 000 grid cells in each model. This grid resolution is sufficient to capture the geometry and connectivity of sketched facies units, and, based on sensitivity tests, to calculate flow diagnostics with reasonable accuracy (i.e. <5% difference in flow diagnostic results compared to higher-resolution models with up to 10 000 000 grid cells); a finer grid brings no significant increase in accuracy of the flow diagnostic results in the models considered here. The time of flight and displacement by injected fluid are calculated between opposing faces of each model, with the other four model faces set as no-flow boundaries. Injection and offtake (production) of tracer fluid take place over an entire model face, rather than in wells, which implies that these model boundaries are open to flow. Displacement by injected fluid is calculated in four directions: (1) up depositional dip, from NE to SW (x_{max} to x_{min}); (2) down depositional dip, from SW to NE (x_{min} to x_{max}); (3) along depositional strike, from NW to SE (y_{max} to y_{min}); and (4) along depositional strike, from SE to NW (y_{min} to y_{max}). Pressure conditions at the model-face boundaries are determined from the distance between opposing model faces, with pressure differentials of 1 MPa between SW and NE faces (along the x-axis) and 0.48 MPa between SE and NW faces (along the y-axis), respectively, in order to maintain a consistent pressure gradient for all four evaluated flow directions. These pressure gradients are chosen principally to investigate migration and storage of an incompressible tracer fluid over the length scale of the model volume, consistent with the use of flow diagnostics, but are comparable to the pressure gradients expected in regions of a CO_2 storage reservoir that are not near to injection wellbores (cf. De Simone and Krevor 2021; Bump and Hovorka 2024). As outlined below, we use a metric to compare fluid migration and storage in different models that normalizes the tracer-fluid injection rate (relative to the pore volume in the model and to the time required for tracer fluid to flow between the open boundaries at opposite faces of the model), such that this comparative metric is independent of the absolute value of pressure differential. For each flow direction, a simulated observation well is placed in the centre of the model face at which injection occurs; this well shares the same pressure conditions as the rest of the model-face boundary at which it is located.

Future work will focus on incorporating the effects of smaller-scale heterogeneities than those considered here, via the use of flow diagnostics to derive effective properties from models that characterize representative elementary volumes of individual facies (cf. Hossain *et al.* 2025). Effective properties for multiphase flow derived from models of the characteristic small-scale heterogeneities in each facies will also be the focus of future work, in order to generate results that are specific to CO_2 and H_2 storage.

Comparison of models

Three metrics are used to compare the volumetric and flow-diagnostic calculations for different models (cf. Jackson *et al.* 2022; Alshakri *et al.* 2023). (1) Total pore volume describes the maximum potential for subsurface fluid storage. We do not use a low-porosity or net-to-gross cut-off(s) to exclude the low permeability units from the calculations of total pore volume. (2) Effective permeability is computed, using flow-based upscaling with no-flow boundaries, over the entire model volume in three orthogonal directions (x, y, z). (3) Pore volume injected (PVI) at breakthrough time provides a proxy for the normalized volume of injected fluid stored in a model due to stratigraphic baffling and trapping. PVI at breakthrough time is computed in each of the four directions described above (i.e. from NE to SW, from SW to NE, from NW to SE and from SE to NW), for tracer fluid between open boundaries at two opposite faces of the model. Snapshots of contacted reservoir volumes at different PVI, which are obtained from the tracer distributions and the time-of-flight field, are also used to visualize flow paths in relation to facies distributions in different models.

Results

Total pore volume

Description

The mean value of total pore volume across the suite of 12 models and 8 sets of porosity and permeability values is 1.27×10^9 m^3 (corresponding to porosity of 22.5%). There is little variation in total pore volume across the suite (Fig. 5a), with a minimum value of 1.18×10^9 m^3 (porosity of 21.0%) for models 4C and 10C (Tables 3 and 4) and a maximum value of 1.35×10^9 m^3 (porosity of 23.9%) for models 5G and 11G (Tables 3 and 4). Most of this variation in porosity (8% around mean value; Fig. 5a) is accounted for by the porosity and permeability values assigned to coastal plain and tidal flat deposits (facies Cp1 + T3) (Table 4), although some variation (2% around mean value; Fig. 5a) is attributed to the thickness of tidal and tidally influenced fluvial channel-fill sandbodies (facies T1, T2) (Table 4), plan-view geometry and distribution of tidally influenced fluvial channel-fill sandbodies (facies T2) (Table 4), and porosity and permeability values assigned to distal lower shoreface and offshore deposits (facies W4 + W5) (Table 4). Porosity values for proximal lower shoreface (facies W3), upper shoreface and foreshore (facies W1 + W2) and tidal channel-fill deposits (facies T1) are not varied in our study.

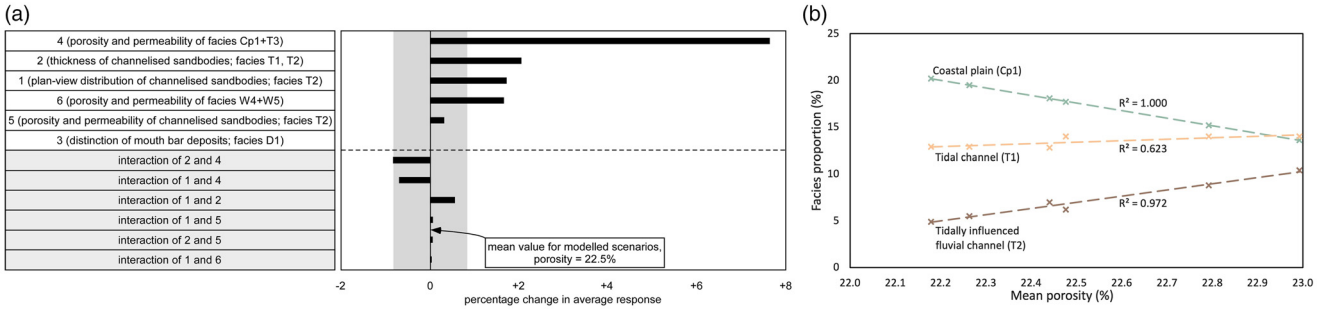

Fig. 5. (**a**) Tornado chart showing the average percentage changes in total pore volume that result from varying each heterogeneity in the 12 models (Table 3) and 8 sets of porosity and permeability values (A–H in Table 4) from its low setting to its high setting. If the bar lies to the right, then the change is positive. Changes in total pore volume are small (<8%) for all heterogeneities. The largest response of confounded two-factor interactions is shown by the grey-shaded region, for comparison with the main effects due to individual factors. (**b**) Linear regression relationships between the mean value of porosity and the proportions of selected facies for the 12 models (Table 3; Fig. 3). R^2 values (coefficient of determination) indicate the goodness of fit of the regression lines to data points.

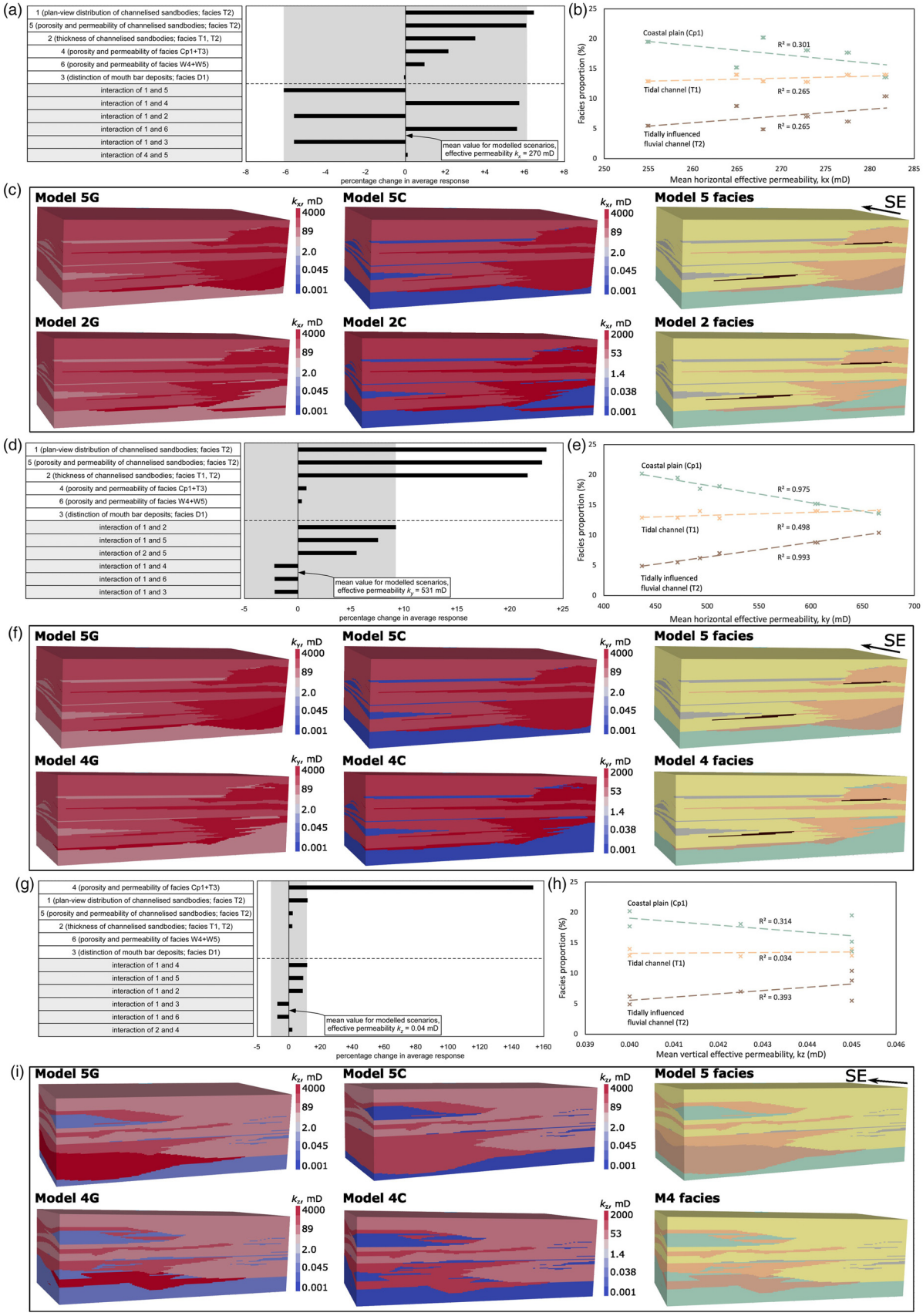

Fig. 6. Comparison of effective permeability in the 12 models (Table 3) and 8 sets of porosity and permeability values (A–H in Table 4). (**a**, **d**, **g**) Tornado charts showing the average percentage changes in values of: (a) effective horizontal permeability in the depositional dip direction, k_x; (d) effective horizontal permeability in the depositional strike direction, k_y; and (g) effective vertical permeability, k_z, that result from varying each heterogeneity from its low setting to its high setting (Tables 3, 4). If the bar lies to the right, then the change is positive. In each tornado chart, the largest response of confounded two-factor interactions is shown by the grey shaded region, for comparison with the main effects due to individual factors. (**b**, **e**, **h**) Linear regression relationships between the proportions of selected facies for the 12 models and the mean value of: (b) k_x; (e) k_y; and (h) k_z. R^2 values (coefficient of determination) indicate the goodness of fit of the regression lines to data points. (**c**, **f**, **i**) 3D perspective views of selected models showing: (c) facies architecture and distribution of facies-specific k_x values; (f) facies architecture and distribution of facies-specific k_y values; and (i) facies architecture and

distribution of facies-specific k_z values. Models are selected because they represent the full range of effective permeability values: (c) models 2G, 2C, 5G and 5C for k_x; (f) models 4G, 4C, 5G and 5C for k_y; and (i) models 2G, 2C, 5G and 5C for k_z. Model dimensions are 10 770 m along depositional dip (NE–SW), 5130 m along depositional strike (NW–SE) and 102 m thick (cf. Fig. 3a). Facies colours in the regression plots and 3D perspective views follow the legend for Figure 2.

Interpretation

The mean value of total pore volume in the 12 models shows a strong negative correlation with the proportion of coastal plain and tidal flat deposits (facies Cp1 + T3) ($R^2 = 1.00$), a strong positive correlation with the proportion of tidally influenced fluvial channel-fill sandbodies (facies T2) ($R^2 = 0.97$), and a moderate positive correlation with the proportion of tidal channel-fill sandbodies (facies T1) ($R^2 = 0.62$) (Fig. 5b). The proportions of other facies either do not vary in the 12 models (facies W1 + W2, W4 + W5) or have only a minor effect on the mean value of total pore volume and are not highlighted in Figure 5b.

Effective permeability

Description

The mean effective permeability values across the suite of 12 models and 8 sets of porosity and permeability values are 270 mD (NE–SW orientation, k_x; Fig. 6a), 531 mD (NW–SE orientation, k_y; Fig. 6d) and 0.04 mD (vertical orientation, k_z; Fig. 6g). Values of k_x vary from 246 mD in model 2C to 295 mD in model 5G (Fig. 6c). Values of k_y tend to be larger than those of k_x, and vary from 400 mD in model 4C to 767 mD in model 5G (Fig. 6f). Values of k_z are much smaller than those of k_x and k_y, and vary from 0.01 mD in models 4C and 5C to 0.08 mD in model 5G (Fig. 6i).

Interpretation

The plan-view geometry and distribution of tidally influenced fluvial channel-fill sandbodies (facies T2) (Table 3; Fig. 4), and the porosity and permeability values assigned to these sandbodies (Table 4) have the greatest influence on values of k_x (6% around mean value; Fig. 6a). Note that the permeability of proximal lower shoreface (facies W3), upper shoreface and foreshore (facies W1 + W2) and tidal channel-fill deposits (facies T1) is not varied. The interactions of the plan-view geometry and distribution of tidally influenced fluvial channel-fill sandbodies (facies T2) with other heterogeneities are also important (Fig. 6a). Mean values of k_x increase progressively from models with scenario 1 of the plan-view distribution and geometry of tidally influenced fluvial channel-fill sandbodies (facies T1) (Fig. 4a, b; models 1, 2, 7, 8 in Table 3) to corresponding models with scenario 2 (Fig. 4c, d; models 3, 4, 9, 10 in Table 3) and scenario 3 (Fig. 4e, f; models 5, 6, 11, 12 in Table 3), reflecting an increase in the up-dip (SW) to down-dip (NE) connectivity of the channelized sandbodies (facies T1). There are only weak correlations between mean values of k_x and the proportions of coastal plain and tidal flat deposits (facies Cp1 + T3) ($R^2 = 0.30$), tidally influenced fluvial channel-fill sandbodies (facies T2) ($R^2 = 0.27$) and tidal channel-fill sandbodies (facies T1) ($R^2 = 0.27$) (Fig. 6b). Thus sandbody connectivity along depositional dip in the suite of models is not controlled predominantly by the proportion of channelized sandbodies, but by their geometry and spatial organization.

The same two heterogeneities, together with the thickness of tidal and tidally influenced fluvial channel-fill sandbodies (facies T1, T2) (Table 4), also control values of k_y (22–23% around mean value; Fig. 6d). Values of k_y increase progressively from models with scenario 2 of the plan-view distribution and geometry of channelized sandbodies (Fig. 4c, d; models 3, 4, 9, 10 in Table 3) to corresponding models with scenario 1 (Fig. 4a, b; models 1, 2, 7, 8 in Table 3) and scenario 3 (Fig. 4e, f; models 5, 6, 11, 12 in Table 3). However, mean values of k_y exhibit moderate-to-strong correlations with the proportions of tidally influenced fluvial channel-fill sandbodies (facies T2) ($R^2 = 0.99$), coastal plain and tidal flat deposits (facies Cp1 + T3) ($R^2 = 0.98$) and tidal channel-fill sandbodies (facies T1) ($R^2 = 0.50$) (Fig. 6e). By implication, sandbody connectivity along depositional strike is controlled predominantly by the proportion of channelized sandbodies.

Values of k_z depend almost entirely on the value of permeability assigned to coastal plain and tidal flat deposits (facies Cp1 + T3) (>150% around mean value; Fig. 6g), and have only weak correlations with facies proportions ($R^2 = 0.03$–0.39; Fig. 6h). Coastal plain and tidal flat deposits (facies Cp1 + T3) form a continuous layer in the lower part of each model (Figs 3, 4 and 6i), which determines k_z. Less laterally continuous lenses and wedges of these deposits, and of distal lower shoreface and offshore deposits (facies W4 + W5) that are also assigned reservoir or non-reservoir properties (Table 4), are present in the upper part of each model (Figs 3, 6i), but exert little influence on k_z.

Pore volume injected at breakthrough

Description

The mean values of PVI at breakthrough vary between the four flow directions within the suite of models. Values are larger for flow along depositional dip, along the longest dimension of the model (Figs 7, 8). For flow up depositional dip (x_{max} to x_{min}), mean values of PVI at breakthrough range from 0.52 (model 11) to 0.74 (model 10), with a mean of 0.64 (Fig. 7a). For flow down depositional dip (x_{min} to x_{max}), mean values of PVI at breakthrough range from 0.46 (model 9) to 0.67 (model 7), with a mean of 0.54 (Fig. 8a). Values are smaller for flow along depositional strike, along the shortest dimension of the model (Figs 9, 10), but there are small differences depending on whether flow is from NW to SE (y_{max} to y_{min}; Fig. 9) or from SE to NW (y_{min} to y_{max}; Fig. 10). Mean values of PVI at breakthrough range from 0.24 (model 10) to 0.31 (model 5), with a mean of 0.27, for flow from NW to SE (y_{max} to y_{min}; Fig. 9a), and from 0.26 (model 9) to 0.32 (model 5), with a mean of 0.29, for flow from SE to NW (y_{min} to y_{max}; Fig. 10a).

Interpretation

For flow up and down depositional dip, most variation in PVI at breakthrough is accounted for by the plan-view geometry and distribution of tidally influenced fluvial channel-fill sandbodies (facies T2) (Table 4), the porosity and permeability values assigned to these sandbodies (facies T2) (Table 4), the thickness of tidal and tidally influenced fluvial channel-fill sandbodies (facies T1, T2) (Table 4), and combinations of these three parameters (Figs 7a, 8a). The connectivity of high-permeability tidal and tidally influenced fluvial channel-fill sandbodies (facies T1, T2) controls flow paths, and thus PVI at breakthrough (Figs 7c–h and 8c–h). Models with low connectivity and/or low permeability of channelized sandbodies exhibit high values of PVI at breakthrough. There are, at best, only weak correlations between mean values of PVI at breakthrough and the proportions of coastal plain and tidal flat deposits (facies Cp1 + T3) ($R^2 = 0.29$–0.30), tidally influenced fluvial channel-fill sandbodies (facies T2) ($R^2 = 0.31$–0.33), and tidal channel-fill sandbodies (facies T1) ($R^2 = 0.05$–0.16) (Figs 7b, 8b). These results are consistent with those for effective permeability along depositional dip, k_x (Fig. 6a–c). Values of PVI at breakthrough are greater for flow up depositional dip (x_{max} to x_{min}) (Fig. 7a) than for flow

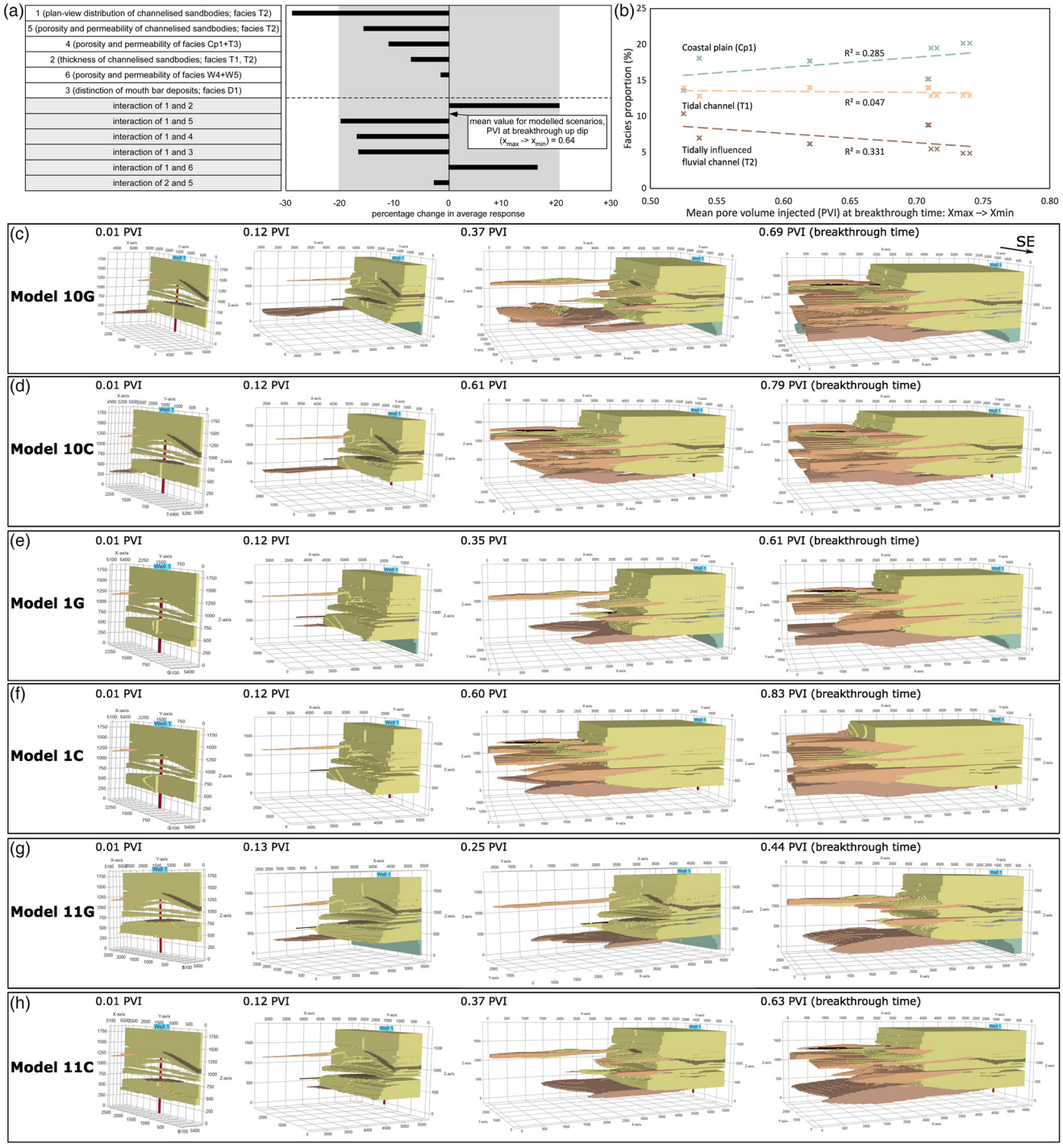

Fig. 7. Comparison of PVI at breakthrough for flow up depositional dip (x_{max} to x_{min}) in the 12 models (Table 3) and 8 sets of porosity and permeability values (A–H in Table 4). (**a**) Tornado chart showing the average percentage changes in values of PVI at breakthrough that result from varying each heterogeneity from its low setting to its high setting (Tables 3, 4). If the bar lies to the right, then the change is positive. The largest response of confounded two-factor interactions is shown by the grey shaded region, for comparison with the main effects due to individual factors. (**b**) Linear regression relationships between the mean value of PVI at breakthrough and proportions of selected facies for the 12 models. R^2 values (coefficient of determination) indicate the goodness of fit of the regression lines to data points. (**c–h**) 3D perspective views of selected models showing snapshots of contacted reservoir volumes for different values of PVI. Models are selected because they represent the full range of PVI at breakthrough values: (c) model 10G; (d) model 10C; (e) model 1G; (f) model 1C; (g) model 11G; and (h) model 11C. Model dimensions are 10 770 m along depositional dip (NE–SW), 5130 m along depositional strike (NW–SE) and 102 m thick (cf. Fig. 3a). The snapshot views show the development of flow paths through high-permeability facies. Facies colours in the regression plots and 3D perspective views follow the legend for Figure 2.

down depositional dip (x_{min} to x_{max}) (Fig. 8a), because high-permeability channelized sandbodies (facies T1, T2) are abundant on the up-dip (SW) face of the model but rarely extend to the down-dip (NE) face of the model (perspective views in Fig. 3a–l). As a result, tracer fluid injected along the down-dip (NE) model face generates a piston-like displacement through lower shoreface sandstones (facies W3) in each parasequence, which are all connected to this face, before being focused through the channelized sandbodies (facies T1, T2) (Fig. 7c–h). In contrast, tracer fluid injected along the up-dip (SW) model face moves rapidly through the channelized sandbodies (facies T1, T2) before sweeping heterogeneously through lower shoreface sandstones

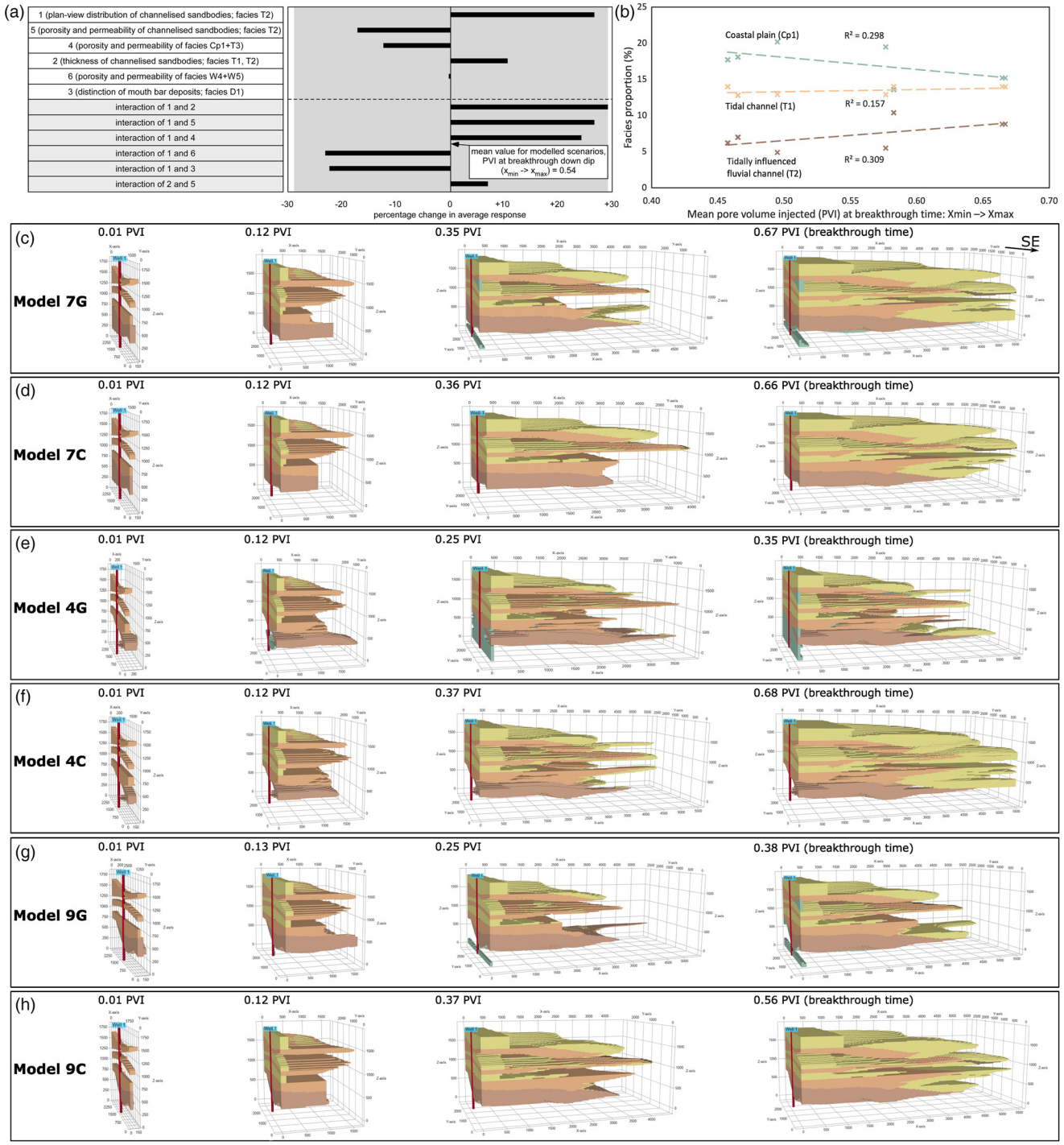

Fig. 8. Comparison of PVI at breakthrough for flow down depositional dip (x_{min} to x_{max}) in the 12 models (Table 3) and 8 sets of porosity and permeability values (A–H in Table 4). (**a**) Tornado chart showing the average percentage changes in values of PVI at breakthrough that result from varying each heterogeneity from its low setting to its high setting (Tables 3, 4). If the bar lies to the right, then the change is positive. The largest response of confounded two-factor interactions is shown by the grey shaded region, for comparison with the main effects due to individual factors. (**b**) Linear regression relationships between the mean value of PVI at breakthrough and proportions of selected facies for the 12 models. R^2 values (coefficient of determination) indicate the goodness of fit of the regression lines to data points. (**c–h**) 3D perspective views of selected models showing snapshots of contacted reservoir volumes for different values of PVI. Models are selected because they represent the full range of PVI at breakthrough values: (c) model 7G; (d) model 7C; (e) model 4G; (f) model 4C; (g) model 9G; and (h) model 9C. Model dimensions are 10 770 m along depositional dip (NE–SW), 5130 m along depositional strike (NW–SE) and 102 m thick (cf. Fig. 3a). The snapshot views show the development of flow paths through high-permeability facies. Facies colours in the regression plots and 3D perspective views follow the legend for Figure 2.

(facies W3) in only those parasequences that occur at the down-dip terminations of the channelized sandbodies (Fig. 8c–h).

Along depositional strike, as along depositional dip, most variation in PVI at breakthrough is accounted for by the plan-view geometry and distribution of tidally influenced fluvial channel-fill sandbodies (facies T2) (Table 4), the porosity and permeability values assigned to these sandbodies (facies T2) (Table 4), the thickness of tidal and tidally influenced fluvial channel-fill sandbodies (facies T1, T2) (Table 4), and combinations of these three parameters (Figs 9a, 10a). Along depositional strike, there is less variation in the connectivity of high-permeability tidal and tidally influenced fluvial channel-fill sandbodies (facies T1, T2),

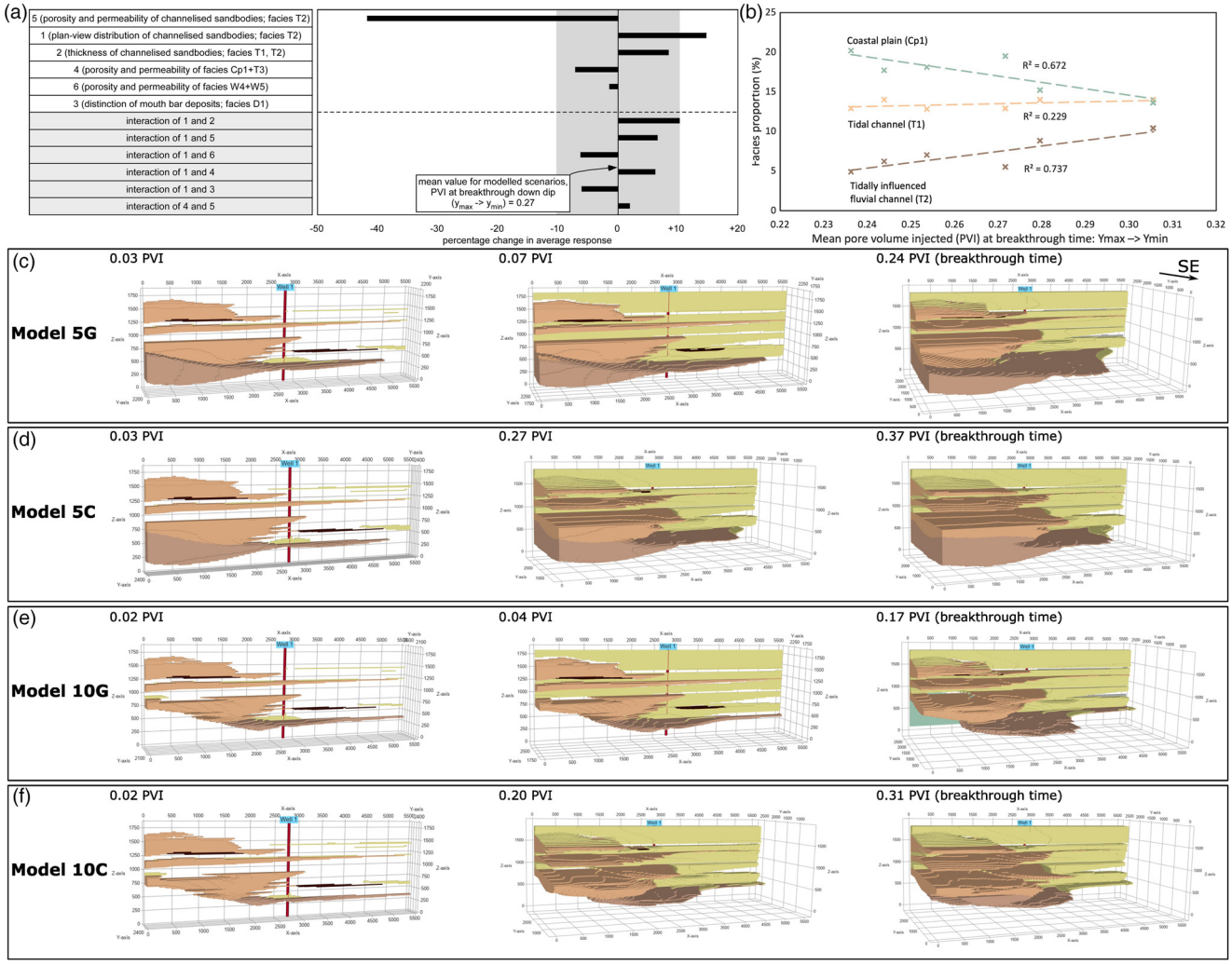

Fig. 9. Comparison of PVI at breakthrough for flow along depositional strike (y_{max} to y_{min}) in the 12 models (Table 3) and 8 sets of porosity and permeability values (A–H in Table 4). (**a**) Tornado chart showing the average percentage changes in values of PVI at breakthrough that result from varying each heterogeneity from its low setting to its high setting (Tables 3, 4). If the bar lies to the right, then the change is positive. The largest response of confounded two-factor interactions is shown by the grey shaded region, for comparison with the main effects due to individual factors. (**b**) Linear regression relationships between the mean value of PVI at breakthrough and proportions of selected facies for the 12 models. R^2 values (coefficient of determination) indicate the goodness of fit of the regression lines to data points. (**c–f**) 3D perspective views of selected models showing snapshots of contacted reservoir volumes for different values of PVI. Models are selected because they represent the full range of PVI at breakthrough values: (c) model 5G; (d) model 5C; (e) model 10G; and (f) model 10C. Model dimensions are 10 770 m along depositional dip (NE–SW), 5130 m along depositional strike (NW–SE) and 102 m thick (cf. Fig. 3a). The snapshot views show the development of flow paths through high-permeability facies. Facies colours in the regression plots and 3D perspective views follow the legend for Figure 2.

such that this parameter is uniformly high and exerts less influence on PVI at breakthrough (Figs 9c–f and 10c–h). There is a corresponding increase in the influence of the proportion of these channelized sandbodies (facies T1, T2) for flow from NW to SE (y_{max} to y_{min}; Fig. 9). In this direction, there are strong correlations between mean values of PVI at breakthrough and the proportions of coastal plain and tidal flat deposits (facies Cp1 + T3) ($R^2 = 0.67$) and tidally influenced fluvial channel-fill sandbodies (facies T2) ($R^2 = 0.74$) (Fig. 9b); this correlation reflects the pronounced variations in the proportions of these high-permeability facies along the NW face of the models, along which tracer is injected (right-hand perspective views in Figs 2a–l and 9c–f). In contrast, the proportion of tidal and tidally influenced fluvial channel-fill sandbodies (facies T1, T2) exerts little influence on flow from SE to NW (y_{min} to y_{max}; Fig. 10). In this direction, there are no correlations between mean values of PVI at breakthrough and the proportions of coastal plain and tidal flat deposits (facies Cp1 + T3) ($R^2 = 0.04$), tidally influenced fluvial channel-fill sandbodies (facies T2) ($R^2 = 0.06$), and tidal channel-fill sandbodies (facies T1) ($R^2 = 0.00$) (Fig. 10b); this lack of correlation reflects the very limited variations in the proportions of these high-permeability facies along the SE face of the models, along which tracer is injected (left-hand perspective views in Figs 2a–l and 10c–h). These results are consistent with those for effective permeability along depositional strike, k_y (Fig. 6d–f), but demonstrate the variation that can result from the exact location of injector and producer faces in our analysis.

Discussion

Which sedimentological heterogeneities control subsurface fluid flow and storage in net-transgressive, shallow-marine sandstones?

Only some of the heterogeneities and settings considered in our models (Tables 3 and 4) have a significant impact on porosity, effective permeability, and/or PVI at breakthrough. There is only a modest range of porosity (21.0–23.9%) and effective permeability (k_x = 246–295 mD; k_y = 400–767 mD; k_z = 0.01–0.08 mD) in the

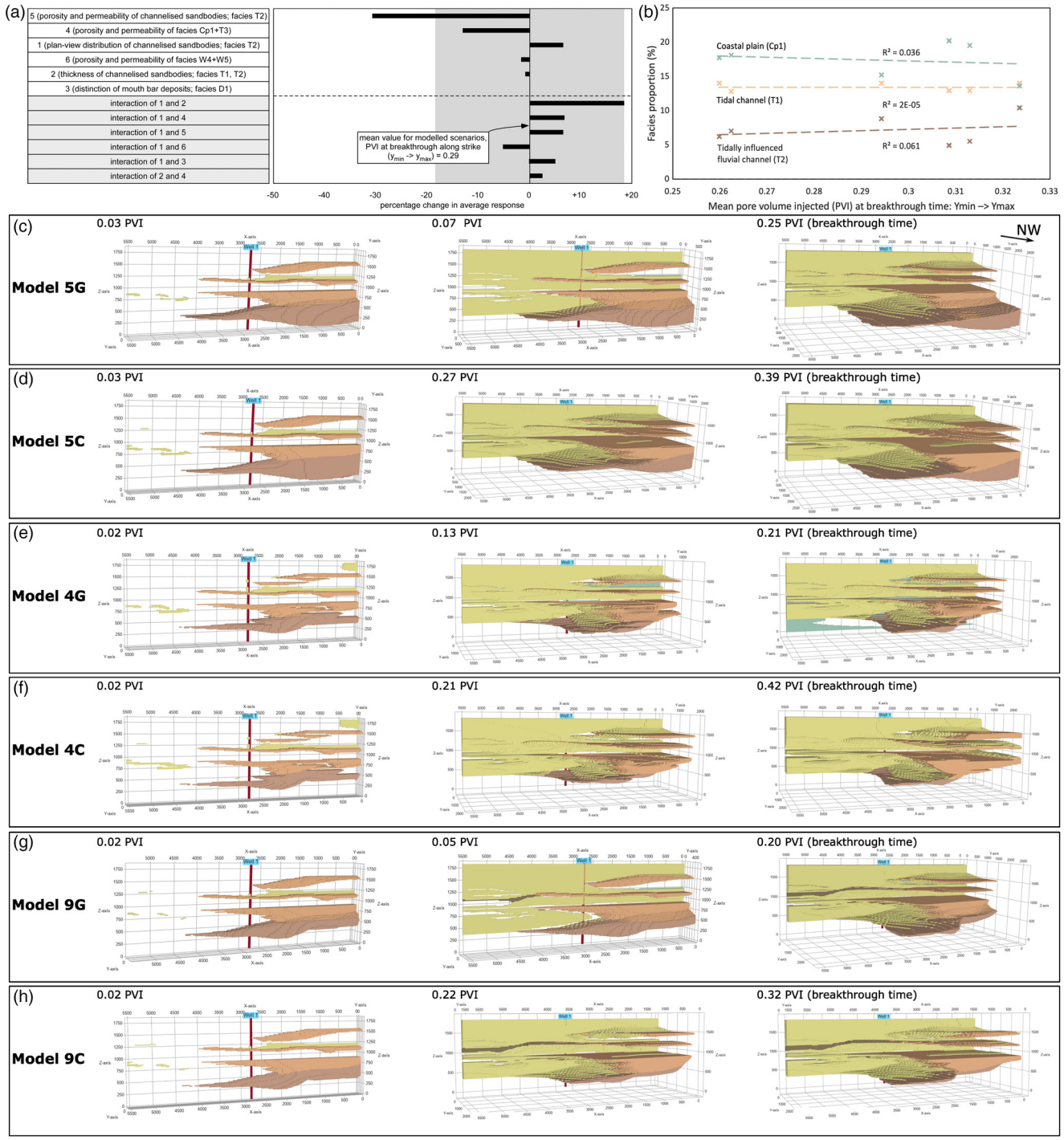

Fig. 10. Comparison of PVI at breakthrough for flow along depositional strike (y_{min} to y_{max}) in the 12 models (Table 3) and 8 sets of porosity and permeability values (A–H in Table 4). (**a**) Tornado chart showing the average percentage changes in values of PVI at breakthrough that result from varying each heterogeneity from its low setting to its high setting (Tables 3, 4). If the bar lies to the right, then the change is positive. The largest response of confounded two-factor interactions is shown by the grey shaded region, for comparison with the main effects due to individual factors. (**b**) Linear regression relationships between the mean value of PVI at breakthrough and proportions of selected facies for the 12 models. R^2 values (coefficient of determination) indicate the goodness of fit of the regression lines to data points. (**c–h**) 3D perspective views of selected models showing snapshots of contacted reservoir volumes for different values of PVI. Models are selected because they represent the full range of PVI at breakthrough values: (c) model 5G; (d) model 5C; (e) model 4G; (f) model 4C; (g) model 9G; and (h) model 9C. Model dimensions are 10 770 m along depositional dip (NE–SW), 5130 m along depositional strike (NW–SE) and 102 m thick (cf. Fig. 3a). The snapshot views show the development of flow paths through high-permeability facies. Facies colours in the regression plots and 3D perspective views follow the legend for Figure 2.

suite of 12 models (Table 3) and 8 sets of porosity and permeability values (Table 4) investigated for the Cliff House Sandstone example. However, this modest variability results in a comparatively large range of associated PVI at breakthrough values (0.35–0.83 along depositional dip; 0.17–0.42 along depositional strike) and associated flow patterns (Figs 7–10). Heterogeneities that have the largest impact on porosity and effective permeability are the plan-view distribution, thickness, and porosity and permeability characteristics of tidal and tidally influenced channel-fill sandbodies (facies T1, T2), and the porosity and permeability characteristics of coastal plain and tidal flat deposits (facies Cp1 + T3) (Figs 5, 6a, d and g).

PVI at breakthrough and associated flow patterns are controlled by the subdivision of shoreface sandstones into laterally extensive parasequences bounded by offshore mudstones in the down-dip, shallow-marine parts of the unit, and by the spatial distributions, connectivity and permeability of channelized sandbodies in the up-dip, marginal-marine parts of the unit (e.g. Figs 7c–h, 8c–h, 9c–h and 10c–h). There is little variability in the thickness, continuity, internal lithological character and fluid-flow patterns of shoreface parasequences along depositional strike (Figs 3, 9c–h and 10c–h), with the transition to localized mouth bar deposits having negligible influence on PVI at breakthrough (Figs 9a, 10a). Where channelized sandbodies are well connected along depositional strike, there is a positive correlation between PVI at breakthrough and the proportion of these sandbodies (Fig. 9b), although this relationship breaks down where channelized sandbodies are poorly connected (Fig. 10b). Variability in flow patterns is more pronounced along depositional dip, reflecting the localized distribution of channelized sandbodies and their connections with shoreface sandstones at the up-dip pinchouts of shoreface parasequences (Figs 3, 7c–h and 8c–h). Flow down depositional dip results in less uniform displacement in shoreface sandstones, and higher values of PVI at breakthrough, because it is more dependent on the localized connections between up-dip channelized sandbodies and down-dip shoreface sandstones (e.g. compare Fig. 7c–h with Fig. 8c–h). Such heterogeneities have been identified previously as important controls on flow patterns and drainage in generic frameworks for hydrocarbon reservoirs (e.g. 'jigsaw puzzle' reservoirs of Weber and Van Geuns 1990), but the detailed stratigraphic architecture and related connectivity between channelized sandbodies and shoreface sheet sandstones are specific to net-transgressive, shallow-marine sandstone reservoirs.

Implications for characterization of subsurface storage reservoirs and sites

As illustrated in Figures 7–10 and discussed above, our results demonstrate that injected tracer fluid is not dispersed uniformly through the Cliff House Sandstone, even though the unit has a high net-to-gross ratio (80–100% for the suite of models illustrated in Fig. 3 and porosity and permeability values listed in Tables 1 and 4). Injected tracer fluid is dispersed in locally variable and anisotropic patterns, particularly through the channelized sandbodies in the up-dip, marginal-marine parts of the unit. The dispersal patterns of specific injected fluids (e.g. supercritical CO_2, warm or cold water) at specific storage sites will be further complicated by the interaction of structural heterogeneities (e.g. tectonic dip, fault juxtaposition and sealing), regional groundwater flow and well placement with the investigated sedimentological heterogeneities (cf. Skorstad *et al.* 2008; Jackson *et al.* 2009), together with the pore-scale interaction of injected and displaced fluid phases with each other and with grain surfaces (Krevor *et al.* 2015; Hashemi *et al.* 2021; Qu *et al.* 2024) and variations in capillary entry pressure associated with centimetre- to decametre-scale heterogeneity (Saadatpoor *et al.* 2009; Gershenzon *et al.* 2016; Jackson and Krevor 2020). Differences in the thermal conductivity of sandstones, mudstones and other rock types will also affect thermal energy storage to a modest extent (e.g. Clauser 2021; Baird *et al.* 2024). Our results thus provide generic insights into the effects of large (metre-to-kilometre) scale sedimentological heterogeneities on subsurface fluid flow and storage, but they need to be extended to include additional heterogeneities, fluid properties and rock-fluid interactions for specific storage sites and projects.

Storage efficiency could be reduced by differential sweep, since less of the available pore space is contacted by the injected fluid (cf. hydrocarbon recovery; Weber and Van Geuns 1990; Tyler and Finley 1991), or increased as a result of stratigraphic trapping at sandbody pinchouts (Flett *et al.* 2007; Gibson-Poole *et al.* 2009), and the areal footprint of the injected-fluid plume may differ from pre-injection predictions that do not account for sedimentological heterogeneity. Given the small thickness of individual shoreface parasequences and channelized sandbodies (<15 m; Figs 2, 3) and the sandstone-dominated character of the unit, it is likely that lithological contrasts will not be seismically imaged in corresponding subsurface strata. Differential fluid saturations and pressures that arise during fluid injection may also lie below the resolution of time-lapse seismic data. Wireline-log and core data from wells could enable the identification of shoreface sandstones in laterally extensive parasequences bounded by offshore mudstones and, where penetrated, of channelized sandbodies in mudstone-dominated marginal-marine strata. However, the spatial distribution and connectivity of channelized sandbodies with each other and with shoreface sandstones are poorly constrained by well data, particularly where wells are widely spaced (e.g. Weber and Van Geuns 1990; Tyler and Finley 1991). The resulting uncertainty in sandbody connectivity and reservoir behaviour can be evaluated by reservoir modelling studies (e.g. Jones *et al.* 1995; Larue and Hovadik 2006; Villamizar *et al.* 2015).

Conclusions

The Cliff House Sandstone is used as a well-documented outcrop example to investigate the impact of sedimentological heterogeneities on subsurface fluid migration and storage potential in net-transgressive, shallow-marine sandstone reservoirs. Previously published cliff-face correlation panels from the Cliff House Sandstone in Chaco Culture National Historical Park, New Mexico, USA are used to construct a suite of sketch-based reservoir models, which are then compared using flow-diagnostic metrics.

The Cliff House Sandstone outcrop example comprises mudstone-dominated coastal plain, lagoonal and tidal flat deposits that contain channelized tidal and tidally influenced fluvial sandbodies, which are overlain by and pass down depositional dip into 11 aggradationally-to-retrogradationally stacked parasequences composed of wave-dominated shoreface sandstones bounded by offshore mudstones. Six sedimentological heterogeneities are investigated: (1) the plan-view distribution and geometry of channelized tidally influenced fluvial sandbodies; (2) the thickness and vertical connectivity of channelized tidal and tidally influenced fluvial sandbodies; (3) the inclusion of mouth bar sandstones distinct from surrounding proximal lower shoreface sandstones; (4) porosity and permeability of mudstone-dominated coastal plain, lagoonal and tidal flat deposits; (5) porosity and permeability of channelized tidally influenced fluvial sandbodies; and (6) porosity and permeability of distal lower shoreface heteroliths and offshore mudstones.

Total pore volume exhibits little variation between the models. Effective horizontal permeability and PVI at breakthrough, a proxy for flow patterns and stratigraphic trapping potential, are controlled predominantly by: (1) the plan-view distribution and geometry of channelized tidally influenced fluvial sandbodies; (2) the porosity and permeability of channelized tidally influenced fluvial sandbodies; and (3) the interactions of these and other heterogeneities. In detail, flow patterns visualized using time-of-flight flow diagnostics are governed by the stratigraphic compartmentalization of shoreface sandstones by parasequence-bounding offshore mudstones; the spatial distribution, connectivity and permeability of channelized sandbodies; and the local positions of connections between channelized sandbodies and shoreface sandstones. Flow up depositional dip results in more uniform displacement in shoreface sandstones in down-dip locations. Flow down depositional dip occurs through channelized sandbodies in up-dip locations, which are variably connected with down-dip shoreface sandstones that are poorly swept as a result. Flow patterns along depositional strike reflect local variations in the connectivity of channelized

sandbodies. Such sandbody connectivity is likely to be poorly constrained in subsurface seismic and well data, and characterization of the resulting uncertainty in subsurface fluid flow and storage potential requires reservoir modelling.

Acknowledgements We are grateful for the constructively critical reviews of Gareth Williams and an anonymous reviewer, and the editorial handling of Philip Ringrose. We thank Oliver Jordan, Sanjeev Gupta and Howard Johnson for discussion of the sedimentology and stratigraphy of the Cliff House Sandstone. We also thank Julio Silva, Sicilia Judice, Fazilatur Rahman, Mario Costa Sousa and members of Phase 1 of the Rapid Reservoir Modelling Consortium (Equinor, ExxonMobil Upstream Research Company, Petrobras, Shell, and IBM Research Brazil/IBM Centre for Advanced Studies (CAS) Alberta, Canada) and Phase 2 of the Rapid Reservoir Modelling Consortium (Equinor, ExxonMobil Upstream Research Company, Petrobras, Petronas and Shell) for discussion of sketch-based modelling. Geiger acknowledges partial funding for his Chair from Energi Simulation, and Jacquemyn and Jackson acknowledge support from EPSRC via the ATESHAC project.

Author contributions **XW**: conceptualization (supporting), investigation (lead), methodology (supporting), writing – original draft (lead); **GJH**: conceptualization (lead), data curation (lead), methodology (lead), supervision (lead), writing – review & editing (equal); **CJ**: conceptualization (supporting), methodology (supporting), supervision (supporting), writing – review & editing (supporting); **SH**: conceptualization (supporting), methodology (supporting), supervision (supporting), writing – review & editing (supporting); **MDJ**: conceptualization (supporting), methodology (supporting), supervision (supporting), writing – review & editing (supporting); **DP**: conceptualization (supporting), methodology (supporting), supervision (supporting), writing – review & editing (supporting); **SG**: methodology (supporting), supervision (supporting), writing – review & editing (supporting).

Funding This research received no specific grant from any funding agency in the public, commercial, or not-for-profit sectors.

Competing interests The authors declare that they have no known competing financial interests or personal relationships that could have appeared to influence the work reported in this paper.

Data availability The geological data used to construct the models is published in Jordan *et al.* (2016). The Rapid Reservoir Modelling prototype (executable and source code) used to construct the models is available at: https://bitbucket.org/rapidreservoirmodelling/rrm. The 12 models used in this study are available at: https://figshare.com/articles/dataset/RRM_models_of_Cliff_House_Sandstone_Chaco_Culture_National_Historical_Park_USA_/25669491?file=45833250.

References

Abbots, F.V. and Van Kuijk, A.D. 1997. Using 3D geological modelling and connectivity analysis to locate remaining oil targets in the Brent reservoir of the mature Brent Field. Paper SPE-38473-MS, presented at the SPE Offshore Europe, Aberdeen, United Kingdom, September 1997, https://doi.org/10.2118/38473-MS

Alshakri, J., Hampson, G.J. *et al.* 2023. A screening assessment of the impact of sedimentological heterogeneity on CO2 migration and stratigraphic-baffling potential: Sherwood and Bunter sandstones, UK. *Geological Society, London, Special Publications*, **528**, 245–266, https://doi.org/10.1144/SP528-2022-34

Baird, K., Arnold, D. *et al.* 2024. Assessment of the impacts of multi-scale sedimentological heterogeneity on low-enthalpy geothermal energy production. Proceedings of 49th Workshop on Geothermal Reservoir Engineering, Stanford Univeristy, California, https://pangea.stanford.edu/ERE/pdf/IGAstandard/SGW/2024/Baird.pdf

Box, G., Hunter, W. and Hunter, J. 1978. *Statistics for Experimenters: An Introduction to Design, Data Analysis, and Model Building*. Wiley Press, New York.

Bump, A.P. and Hovorka, S.D. 2024. Pressure space: the key subsurface commodity for CCS. *International Journal of Greenhouse Gas Control*, **136**, 104174, https://doi.org/10.1016/j.ijggc.2024.104174

Cattaneo, A. and Steel, R.J. 2003. Transgressive deposits, a review of their variability. *Earth Science Reviews*, **62**, 187–223, https://doi.org/10.1016/S0012-8252(02)00134-4

Caumon, G., Collon-Drouaillet, P., Le Carlier de Veslud, C., Viseur, S. and Sausse, J. 2009. Surface-based 3D modeling of geological structures. *Mathematical Geosciences*, **41**, 927–945, https://doi.org/10.1007/s11004-009-9244-2

Clauser, C. 2021. Thermal storage and transport properties of rocks, II: thermal conductivity and diffusivity. *In:* Gupta, H.K. (ed.) *Encyclopedia of Solid Earth Geophysics*. 2nd edn. Springer International Publishing, Cham, 1769–1787, https://doi.org/10.1007/978-3-030-58631-7_67

Colombera, L. and Mountney, N.P. 2021. Influence of fluvial crevasse-splay deposits on sandbody connectivity: lessons from geological analogues and stochastic modelling. *Marine and Petroleum Geology*, **128**, 105060, https://doi.org/10.1016/j.marpetgeo.2021.105060

Copestake, P. 2023. Chapter 9. Application of sequence stratigraphy to the evaluation of selected North Sea Jurassic hydrocarbon fields and carbon capture, utilization and storage (CCUS) projects. *Geological Society of London, Memoir*, **59**, 249–291, https://doi.org/10.1144/M59-2022-59

Costa Sousa, M., Silva, J.D.M. *et al.* 2020. Smart modelling of geologic stratigraphy concepts using sketches. Smart Tools and Applications in computer Graphics (STAG) 2020 Proceedings, 12–13 November, online, 89–100, https://doi.org/10.2312/stag.20201243

Crooijmans, R.A., Willems, C.J.L., Nick, H.M. and Bruhn, D.F. 2016. The influence of facies heterogeneity on the doublet performance in low-enthalpy geothermal sedimentary reservoirs. *Geothermics*, **64**, 209–219, https://doi.org/10.1016/j.geothermics.2016.06.004

Denver, L.E. and Phillips, D.C. 1990. Stratigraphic geocellular modeling. *Geobyte*, **5**, 45–47.

De Simone, S. and Krevor, S. 2021. A tool for first order estimates and optimisation of dynamic storage resource resource in saline aquifers. *International Journal of Greenhouse Gas Control*, **106**, 103258, https://doi.org/10.1016/j.ijggc.2021.103258

Donselaar, M.E. 1989. The Cliff House Sandstone, San Juan Basin, New Mexico; model for the stacking of "transgressive" barrier complexes. *Journal of Sedimentary Research*, **59**, 13–27, https://doi.org/10.1306/212f8f08-2b24-11d7-8648000102c1865d

Flett, M., Gurton, R. and Weir, G. 2007. Heterogeneous saline formations for carbon dioxide disposal: impact of varying heterogeneity on containment and trapping. *Journal of Petroleum Science and Engineering*, **57**, 106–118, https://doi.org/10.1016/j.petrol.2006.08.016

Gershenzon, N.I., Ritzi, R.W., Dominic, D.F., Mehnert, E. and Okwen, R.T. 2016. Comparison of CO_2 trapping in highly heterogeneous reservoirs with Brooks-Corey and van Genuchten type capillary pressure curves. *Advances in Water Resources*, **96**, 225–236, https://doi.org/10.1016/j.advwatres.2016.07.022

Gibling, M.R. 2006. Width and thickness of fluvial channel bodies and valley fills in the geological record: a literature compilation and classification. *Journal of Sedimentary Research*, **76**, 731–770, https://doi.org/10.2110/jsr.2006.060

Gibson-Poole, C.M., Svendsen, L., Watson, M.N., Daniel, R.F., Ennis-King, J. and Rigg, A.J. 2009. Understanding stratigraphic heterogeneity: a methodology to maximize the efficiency of the geological storage of CO_2. *American Association of Petroleum Geologists, Studies in Geology*, **59**, 347–364, https://doi.org/10.1306/13171248St593385

Goh, L.S. 1993. The Logger field: geology and reservoir characterization. *In:* Aasen, J.O., Buller, A.T., Hjelmeland, O., Holt, R.M., Kleppe, J. and Torsæter, O. (eds) *North Sea Oil and Gas Reservoirs – III: Proceedings of the 3rd North Sea Oil and Gas Reservoirs Conference*. Kluwer Academic Publishers, Dordrecht, 75–93.

Hamilton, D.E. and Jones, T.A. 1992. *Computer Modeling of Geologic Surfaces and Volumes*. *American Association of Petroleum Geologists, Computer Applications in Geology*, **1**.

Hampson, G.J., Sixsmith, P.J., Kieft, R.L., Jackson, C.A.L. and Johnson, H.D. 2009. Quantitative analysis of net-transgressive shoreline trajectories and stratigraphic architectures: mid-to-late Jurassic of the North Sea Rift Basin. *Basin Research*, **21**, 528–558, https://doi.org/10.1111/j.1365-2117.2009.00414.x

Hashemi, L., Blunt, M. and Hajibeygi, H. 2021. Pore-scale modelling and sensitivity analyses of hydrogen-brine multiphase flow in geological porous media. *Scientific Reports*, **11**, 8348, https://doi.org/10.1038/s41598-021-87490-7

Hossain, S., Hampson, G.J. *et al.* 2025. Effective permeability of fluvial lithofacies in the Bunter Sandstone Formation, UK. *Advances in Water Resources*, 199, 104936, https://doi.org/10.1016/j.advwatres.2025.104936

Howell, J.A., Martinius, A.W. and Good, T.R. 2014. The application of outcrop analogues in geological modelling: a review, present status and future outlook. *Geological Society, London, Special Publications*, **387**, 1–25, https://doi.org/10.1144/SP387

Jackson, M.D., Hampson, G.J. and Sech, R.P. 2009. Three-dimensional modeling of a shoreface-shelf parasequence reservoir analog: part 2. Geologic controls on fluid flow and hydrocarbon recovery. *American Association of Petroleum Geologists Bulletin*, **93**, 1183–1208, https://doi.org/10.1306/05110908145

Jackson, S.J. and Krevor, S. 2020. Small-scale capillary heterogeneity linked to rapid plume migration during CO_2 storage. *Geophysical Research Letters*, **47**, e2020GL088616, https://doi.org/10.1029/2020GL088616

Jackson, W.A., Hampson, G.J. *et al.* 2022. A screening assessment of the impact of sedimentological heterogeneity on CO_2 migration and stratigraphic-baffling potential: Johansen and Cook formations, Northern Lights project, offshore Norway. *International Journal of Greenhouse Gas Control*, **120**, 103762, https://doi.org/10.1016/j.ijggc.2022.103762

Jacquemyn, C., Jackson, M.D. and Hampson, G.J. 2019. Surface-based geological reservoir modelling using grid-free NURBS curves and surfaces.

Mathematical Geosciences, **51**, 1–28, https://doi.org/10.1007/s11004-018-9764-8

Jacquemyn, C., Pataki, M.E.H. *et al.* 2021. Sketch-based interface and modelling of stratigraphy and structure in three dimensions. *Journal of the Geological Society, London*, **178**, jgs2020-187, https://doi.org/10.1144/jgs2020-187

Jones, A.D.W., Doyle, J.D., Jacobsen, T. and Kjønsvik, D. 1995. Which sub-seismic heterogeneities influence waterflood performance? A case study of a low net-to-gross fluvial reservoir. *Geological Society, London, Special Publications*, **84**, 5–18, https://doi.org/10.1144/GSL.SP.1995.084.01.02

Jordan, O.D., Gupta, S., Hampson, G.J. and Johnson, H.D. 2016. Preserved stratigraphic architecture and evolution of a net-transgressive mixed wave- and tide-influenced coastal system: the Cliff House Sandstone, Northwestern New Mexico, USA. *Journal of Sedimentary Research*, **86**, 1399–1424, https://doi.org/10.2110/jsr.2016.83

Kauffman, E.G. and Caldwell, W.G.E. 1993. The Western Interior Basin in space and time. *Geological Association of Canada Special Paper*, **39**, 1–30.

Krevor, S., Blunt, M.J., Benson, S.M., Pentland, C.H., Reynolds, C., Al-Menhali, A. and Niu, B. 2015. Capillary trapping for geologic carbon dioxide storage – from pore scale physics to field scale implications. *International Journal of Greenhouse Gas Control*, **40**, 221–237, https://doi.org/10.1016/j.ijggc.2015.04.006

Krevor, S., de Coninck, H. *et al.* 2023. Subsurface carbon dioxide and hydrogen storage for a sustainable energy future. *Nature Reviews Earth & Environment*, **4**, 102–118, https://doi.org/10.1038/s43017-022-00376-8

Krystinik, L.F. and DeJarnett, B.B. 1995. Lateral variability of sequence stratigraphic framework in the Campanian and Lower Maastrichtian of the Western Interior Seaway. *Association of Petroleum Geologists, Memoir*, **64**, 11–26, https://doi.org/10.1306/M64594C2

Larue, D.K. and Hovadik, J. 2006. Connectivity of channelized reservoirs: a modelling approach. *Petroleum Geoscience*, **12**, 291–308, https://doi.org/10.1144/1354-079306-699

Lawton, T.F., Pollock, S.L. and Robinson, R.A.J. 2003. Integrating sandstone petrology and nonmarine sequence stratigraphy: application to the Late Cretaceous fluvial systems of southwestern Utah, USA. *Journal of Sedimentary Research*, **73**, 389–406, https://doi.org/10.1306/100702730389

Li, Z. and Aschoff, J. 2022. Shoreline evolution in the Late Cretaceous North American Cordilleran foreland basin: an exemplar of the combined influence of tectonics, sea level, and sediment supply through time. *Earth-Science Reviews*, **226**, 103947, https://doi.org/10.1016/j.earscirev.2022.103947

Lie, K.A., Møyner, O. and Krogstad, S. 2015. Application of flow diagnostics and multiscale methods for reservoir management. Society of Petroleum Engineers, Reservoir Simulation Symposium, Houston, TX, Paper 173376.

Livera, S.E. 1989. Facies associations and sand-body geometries in the Ness Formation of the Brent Group, Brent Field. *Geological Society, London, Special Publications*, **41**, 269–286, https://doi.org/10.1144/GSL.SP.1989.041.01.19

Mijnlieff, H.F. 2020. Introduction to the geothermal play and reservoir geology of the Netherlands. *Netherlands Journal of Geosciences*, **99**, e2, https://doi.org/10.1017/njg.2020.2

Molenaar, C.M. 1983. Major depositional cycles and regional correlations of Upper Cretaceous rocks, southern Colorado Plateau, and adjacent area. *In:* Reynolds, M.W. and Dolly, E.D. (eds) *Mesozoic Paleogeography of West-Central United States. Rocky Mountain Palaeogeography Symposium Vol. 2*, Rocky Mountain Section Society of Economic Paleontologists and Mineralogists, 201–224.

Møyner, O., Krogstad, S. and Lie, K.A. 2014. The application of flow diagnostics for reservoir management. *Society of Petroleum Engineers Journal*, **20**, 306–323, https://doi.org/10.2118/171557-PA

Olsen, T.R., Mellere, D. and Olsen, T. 1999. Facies architecture and geometry of landward-stepping shoreface tongues: the Upper Cretaceous Cliff House Sandstone (Mancos Canyon, south-west Colorado). *Sedimentology*, **46**, 603–625, https://doi.org/10.1046/j.1365-3091.1999.00234.x

Onyenanu, G.I., Hampson, G.J., Fitch, P.J.R. and Jackson, M.D. 2019. Effects of erosional scours on reservoir properties of heterolithic, distal lower-shoreface sandstones. *Petroleum Geoscience*, **25**, 235–248, https://doi.org/10.1144/petgeo2018-058

Painter, C.S. and Carrapa, B. 2013. Flexural versus dynamic processes of subsidence in the North American Cordillera foreland basin. *Geophysical Research Letters*, **40**, 4249–4253, https://doi.org/10.1002/grl.50831

Palmer, J.J. and Scott, A.J. 1984. Stacked shoreline and shelf sandstone of La Ventena Tongue (Campanian), northwestern New Mexico. *American Association of Petroleum Geologists Bulletin*, **68**, 74–91, https://doi.org/10.1306/AD46096D-16F7-11D7-8645000102C1865D

Petrovskyy, D., Jacquemyn, C.E.M.M. *et al.* 2023. Rapid flow diagnostics for reservoir prototyping - applications to subsurface CO_2 storage. *International Journal of Greenhouse Gas Control*, **124**, 103855, https://doi.org/10.1016/j.ijggc.2023.103855

Pyrcz, M.J., Catuneanu, O. and Deutsch, C.V. 2005. Stochastic surface-based modeling of turbidite lobes. *American Association of Petroleum Geologists Bulletin*, **89**, 177–191, https://doi.org/10.1306/09220403112

Qu, M.L., Yang, J., Foroughi, S., Zhang, Y., Yu, Z.T., Blunt, M.J. and Lin, Q. 2024. Pore-to-meter scale modeling of heat and mass transport applied to thermal energy storage: how local thermal and velocity fluctuations affect average thermal dispersivity. *Energy*, **296**, 131147, https://doi.org/10.1016/j.energy.2024.131147

Rasmussen, A. and Lie, K.A. 2014. Discretization of flow diagnostics on stratigraphic and unstructured grids. 14th European Conference on the Mathematics of Oil Recovery, Catania, Sicily, 1–17, https://doi.org/10.3997/2214-4609.20141844

Ruiu, J., Caumon, G. and Viseur, S. 2016. Modeling channel forms and related sedimentary objects using a boundary representation based on non-uniform rational B-splines. *Mathematical Geosciences*, **48**, 259–284, https://doi.org/10.1007/s11004-015-9629-3

Saadatpoor, E., Bryant, S.L. and Sepehrnoori, K. 2009. New trapping mechanism in carbon sequestration. *Transport in Porous Media*, **82**, 3–17, https://doi.org/10.1007/s11242-009-9446-6

Scott, G.R., O'Sullivan, R.B. and Weide, D.L. 1984. *Geologic Map of the Chaco Culture National Historical Park, North Western New Mexico*. *United States Geological Survey Miscellaneous Investigations Series Map*, **I-1571**, 1 sheet, scale 1:50,000.

Sears, J.D., Hunt, C.B. and Hendricks, T.A. 1941. *Transgressive and Regressive Cretaceous Deposits in Southern San Juan Basin, New Mexico*. *United States Geological Survey, Professional Paper*, **193-F**.

Sech, R.P., Jackson, M.D. and Hampson, G.J. 2009. Three-dimensional modeling of a shoreface-shelf parasequence reservoir analog: part 1. Surface-based modeling to capture high-resolution facies architecture. *Association of Petroleum Geologists Bulletin*, **93**, 1155–1181, https://doi.org/10.1306/05110908144

Shahvali, M., Mallison, B., Wei, K. and Gross, H. 2012. An alternative to streamlines for flow diagnostics on structured and unstructured grids. *Society of Petroleum Engineers Journal*, **17**, 768–778, https://doi.org/10.2118/146446-PA

Siebels, A., Bults, A., Nolten, M., Wierenga, J., Doust, H. and Verbeek, J. 2022. Potential for CO_2 sequestration in saline formations in the western offshore Netherlands: a preliminary study – expanding carbon capture and storage beyond depleted fields. *American Association of Petroleum Geologists Bulletin*, **106**, 1855–1876, https://doi.org/10.1306/02252221018

Sixsmith, P.J., Hampson, G.J., Gupta, S., Johnson, H.D. and Fofana, J.F. 2008. Facies architecture of a net transgressive sandstone reservoir analog: the Cretaceous Hosta Tongue, New Mexico. *American Association of Petroleum Geologists Bulletin*, **92**, 513–547, https://doi.org/10.1306/01020807017

Skorstad, A., Kolbjørnsen, O., Manzocchi, T., Carter, J.N. and Howell, J.A. 2008. Combined effects of structural, stratigraphic and well controls on production variability in faulted shallow-marine reservoirs. *Petroleum Geoscience*, **14**, 45–54, https://doi.org/10.1144/1354-079307-789

Swift, D.J.P. 1968. Coastal erosion and transgressive stratigraphy. *Journal of Geology*, **76**, 444–456, https://doi.org/10.1086/627342

Szwarc, T.S., Johnson, C.L., Stright, L.E. and McFarlane, C.M. 2015. Interactions between axial and transverse drainage systems in the Late Cretaceous Cordilleran foreland basin: evidence from detrital zircons in the Straight Cliffs Formation, southern Utah, USA. *Geological Society of America Bulletin*, **127**, 372–392, https://doi.org/10.1130/B31039.1

Taylor, A.M. and Goldring, R. 1993. Description and analysis of bioturbation and ichnofabric. *Journal of the Geological Society, London*, **150**, 141–148, https://doi.org/10.1144/gsjgs.150.1.0141

Tyler, N. and Finley, R.J. 1991. Architectural controls on the recovery of hydrocarbons from sandstone reservoirs. *In:* Miall, A.D. and Tyler, N. (eds) *The Three-Dimensional Facies Architecture of Terrigenous Clastic Sediments and Its Implications for Hydrocarbon Recovery and Discovery*. *Society for Sedimentary Geology (SEPM), Concepts in Sedimentology and Paleontology*, **3**, 1–5, https://doi.org/10.2110/csp.91.03.0001

Van Cappelle, M., Hampson, G.J. and Johnson, H.D. 2018. Spatial and temporal evolution of coastal depositional systems and regional depositional process regimes: Campanian Western Interior Seaway, USA. *Journal of Sedimentary Research*, **88**, 873–897, https://doi.org/10.2110/jsr.2018.49

Villamizar, C.A., Hampson, G.J., Flood, Y.S. and Fitch, P.J.R. 2015. Object-based modelling of avulsion-generated sandbody distributions and connectivity in a fluvial reservoir analogue of low to moderate net-to-gross ratio. *Petroleum Geoscience*, **21**, 249–270, https://doi.org/10.1144/petgeo2015-004

Wang, Y., Voskov, D., Khait, M., Saeid, S. and Bruhn, D. 2021. Influential factors on the development of a low-enthalpy geothermal reservoir: a sensitivity study of a realistic field. *Renewable Energy*, **179**, 641–651, https://doi.org/10.1016/j.renene.2021.07.017

Weber, K.J. and Van Geuns, L.C. 1990. Framework for constructing clastic reservoir simulation models. *Journal of Petroleum Technology*, **42**, 1248–1297, https://doi.org/10.2118/19582-PA